universe

MDPI

Article

Constraints on the Gravitational Potential from DESI DR2 BAO and Its Implications for the Local Void Scenario

Indranil Banik *, José Antonio Nájera and Harry Desmond

Institute of Cosmology and Gravitation, University of Portsmouth, Dennis Sciama Building, Burnaby Road, Portsmouth PO1 3FX, UK; antonio.najera@port.ac.uk (J.A.N.); harry.desmond@port.ac.uk (H.D.)
* Correspondence: indranilbanik1992@gmail.com

Abstract

We constrain the difference in gravitational potential between our location and sources at $z \gtrsim 0.3$ using datasets at those redshifts. Our motivation is that the Hubble tension might be caused by a local void, as suggested by galaxy number counts. This would increase the redshift through outflow and gravitational redshift (GR). Only the latter is important at high redshift, where a void contributes a fixed additional GR contribution of z_0 due to our location on a potential hill. This z_0 model has various subtle effects that were not previously considered, including a hotter CMB and reduced BAO scale r_d. We test whether z_0 can have the previously expected value of 0.84%, which was based on the fitting of void parameters to galaxy number counts and local H_0 measurements. Combining BBN, CMB, BAO, and CC datasets at $z > 0.5$, we find that $z_0 = -0.4^{+0.8}_{-0.9}\%$, which rises to $-0.1 \pm 0.7\%$ when extending our analysis down to $z > 0.29$. Although the results prefer the standard value of $z_0 = 0$, the best-fitting model with $z_0 = 0.84\%$ fits the data almost as well as ΛCDM, with $\Delta\chi^2 < 2$. We find that ΛCDM faces a 3.07σ BAO anomaly in the standard $(H_0 r_\mathrm{d}, \Omega_\mathrm{m})$ parameter space, where different regions are preferred by BAO and non-BAO datasets from $z > 0.29$. Fixing $z_0 = 0.84\%$ reduces this to 2.79σ. This suggests that a local void large enough to solve the Hubble tension cannot be ruled out by higher-redshift datasets, despite its novel impacts on them.

Keywords: cosmological parameters; cosmology: theory; cosmology: observations; distance scale; large-scale structure of the Universe; gravitation

1. Introduction

Although it has been clear for over a century that the Universe is expanding [1,2], the present rate of expansion remains a topic of major controversy known as the Hubble tension [3,4]. This arises due to a mismatch between the observed rate at which redshift (z) increases with distance (r) in the local Universe and the predicted rate of increase in the Lambda cold dark matter (ΛCDM) standard cosmological paradigm [5,6] calibrated using observations of the early Universe. If the Universe is taken to be homogeneous and isotropic, it must hold that

$$cz' = \dot{a} = H_0\,, \tag{1}$$

where c is the speed of light, $z' \equiv \mathrm{d}z/\mathrm{d}r$ in the local Universe, a is the cosmic scale factor normalised to unity today, overdots denote time derivatives, 0 subscripts denote quantities at the present epoch, and $H \equiv \dot{a}/a$ is the Hubble parameter [7].

Check for updates

Academic Editor: Anzhong Wang

Received: 26 May 2026
Revised: 14 July 2026
Accepted: 27 July 2026
Published: 6 August 2026

Copyright: © 2026 by the authors. Licensee MDPI, Basel, Switzerland. This article is an open access article distributed under the terms and conditions of the Creative Commons Attribution (CC BY) license.

We can predict H_0 from unrelated observations in several ways, but the technique most commonly used nowadays involves fitting the precisely observed power spectrum of anisotropies in the cosmic microwave background (CMB) using the ΛCDM model. The power spectrum has characteristic oscillatory features, which provide a wealth of information about the baryon–photon plasma in the primordial Universe [8,9]. Modern observations cover up to ten peaks in the CMB power spectrum [10–12]. This is enough to fix the ΛCDM parameters to high precision, leading to a clear prediction that $H_0 = H_0^{\rm CMB} = 67.19 \pm 0.38$ km/s/Mpc [12].

This precise prediction is in $>7\sigma$ tension with the "community consensus" estimate of $cz' = 73.50 \pm 0.81$ km/s/Mpc reported recently by the H_0 Distance Network Collaboration [4]. This estimate combines several popular methods and takes into account their covariances, though it does not properly account for selection effects and homogeneous Malmquist bias, the larger volume per unit distance at larger distances due to sources being distributed in 3D [13–15]. A wide variety of different techniques to construct the local distance ladder give numerically similar estimates of cz' [16]. The most precise results rely on using the period–luminosity relation or Leavitt Law of Cepheid variable stars [17] to calibrate Type Ia supernovae (SNe Ia), which are then assumed to be physically similar out to $z = 0.15$ [18,19]. Single-step techniques such as the use of masers [20,21] and Type II SNe [22] have also been claimed to produce cz' values above $H_0^{\rm CMB}$. This is also the case with a two-rung geometry-to-Cepheids ladder [14]. For a comprehensive review of the Hubble tension and possible solutions, we refer the reader to Di Valentino et al. [3].

Given the evidence that $cz' > H_0^{\rm CMB}$, many workers have tried to find a way to explain the CMB anisotropies in a cosmology with higher H_0 values, for instance, with early dark energy [23,24] or primordial magnetic fields [25]. Whatever the precise details, the lack of new physics in the late Universe implies that $\dot{a}(z)$ should be 9% above that predicted by the CMB-calibrated ΛCDM cosmology for $z \lesssim 1000$. This generic prediction runs into several difficulties. For instance, a faster expansion rate throughout nearly the entirety of cosmic history would reduce the age of the Universe from the usual 13.8 Gyr down to ≈13.8/1.09 = 12.7 Gyr [26]. This is inconsistent with the ages of the oldest Galactic stars and globular clusters [26–41]. While these results are based on absolute stellar ages, similar conclusions can be drawn from differential ages between galaxies at different redshifts [42,43]. In general, probes of the expansion rate at intermediate epochs line up well with the *Planck* cosmology (for a review, see [44]). Moreover, one might expect that substantial changes to pre-recombination physics would distort the CMB power spectrum in some way. However, there are no anomalies in the CMB power spectrum that might be associated with the hypothesised new physics prior to recombination [10,12,45,46]. There are several additional challenges to this approach [47], which may also introduce some tension with Big Bang nucleosynthesis (BBN), given that CMB fits with higher H_0 values are usually associated with a higher baryon density [48,49].

Since the CMB only probes the late Universe through the comoving distance to recombination, it is possible to distort the expansion history such that this integral constraint is preserved but H_0 is higher. A crucial constraint on such models is baryon acoustic oscillation (BAO) measurements from the DESI data release 2 (DESI DR2; [50]). The BAO provides a standard statistical ruler whose comoving size ($r_{\rm d}$) was fixed by the sound horizon at early times [8,9]. By observing the angular scale and redshift depth of the BAO ruler, we can place tight constraints on the expansion history at intermediate epochs [51,52]. A recent exploration of several background solutions to the Hubble tension found that all the considered models struggle when confronted with the BAO [53]. The more physically motivated models generally struggled more, while the phenomenological ("Phen") models performed better. A major result is that the Phen models can succeed to a large extent, but

the deviation from ΛCDM behaviour should be restricted to rather low redshifts, far below the scale where dark energy causes $\ddot{a}$ to switch sign. It is unclear why $H(z)$ would start deviating from ΛCDM only at such low redshifts after working well for billions of years. This would require very unusual behaviour for the dark energy equation of state in the context of General Relativity, though the empirically reconstructed behaviour might be natural in some modified gravity theory.

Given these difficulties with solving the Hubble tension through new physics prior to recombination or a modified background expansion history at late times, we must seriously question the validity of Equation (1), the only common thread in all the proposals mentioned above. The only way to violate Equation (1) is if some of the observed redshift arises from sources other than homogeneous cosmic expansion. cz' can be inflated if there are outward peculiar velocities or we are located on a potential hill, creating gravitational redshift (GR) contributions as photons from the distant Universe struggle against gravity to reach our detectors (Equation (1) of [54]). Both arguments require that we live in a local underdensity or void. While these non-cosmological contributions to z would generally decay as we get to larger redshift, an increasing trend is possible over a limited range of radii, depending on the void properties and our vantage point. A void of the required size and depth is not possible in ΛCDM, which predicts too little cosmic variance in cz' to explain the Hubble tension this way [55,56]. Therefore, the local void scenario still requires new physics—but not at the background level. The main requirement is enhanced growth of structure on scales of $\gtrsim$100 Mpc, which we suggest is related to a modified behaviour of gravity on these scales.

Unlike most solutions to the Hubble tension, which were proposed only after it became apparent, a local void was proposed many decades prior based on optical galaxy number counts [57,58]. The void was later claimed in near-infrared observations covering 90% of the sky, which suggest that we live inside the Keenan–Barger–Cowie (KBC) void [59]. There is evidence for the KBC void across the electromagnetic spectrum, from X-rays [60,61] to radio wavelengths [62,63] and in the infrared band [59,64–71]. Since the underlying observable is the galaxy luminosity density or source number density in redshift space, these results are not dependent on what value is assumed for the local cz'. The increasing comoving luminosity density towards larger redshift is difficult to understand through selection effects, which would instead be expected to favour the detection of nearby galaxies. The observations can be understood in a homogeneous Universe only if we assume extreme evolution of the galaxy population at $z \lesssim 0.1$, followed by much milder evolution out to $z = 1$ [71]. Another argument for a local underdensity is that the mass fraction of galaxies residing in their stellar haloes increases with redshift [72]. Because this halo fraction traces the merger history of galaxies, it can serve as a probe of the local galaxy-number density, as noted by those authors.

The local void scenario was explored in some detail by [73]. Those authors evolved a semi-analytic model of a small initial underdensity from $z = 9$ to the present, enhancing the gravitational field using an approach inspired by Milgromian dynamics (MOND; [74]). It proved possible to obtain a joint fit to the local cz' and the redshift-space comoving density profile of the KBC void, whose apparent density contrast in redshift space is inconsistent with ΛCDM expectations at $>6\sigma$ confidence [73]. More recently, their best-fitting models were claimed to provide a good match to BAO observations over the last 20 years [52]. One can conversely infer the existence of a local void similar to that claimed by Keenan et al. [59] without using galaxy number counts if a background *Planck* cosmology is assumed and local cz' constraints are applied [75]. These and other studies on the local void model were recently reviewed in Banik et al. [76].

Just like background solutions to the Hubble tension, a local void would necessarily introduce 'spillover' effects at high redshift, by which we mean that some impact on cosmology is inevitable besides inflating the local cz'. Our main goal in this contribution is to check if the predicted spillover effects of a local void are consistent with the latest observations, which by now are quite precise yet remain close to ΛCDM expectations. While some of the effects we will consider have been previously discussed [73], they have not been calculated in detail or compared to the latest observations, while other effects have not been recognised. This is crucial in addressing high-precision BAO observations, which were claimed to provide strong support for the [73] void model compared to the homogeneous *Planck* cosmology [52]. However, we identify several major deficiencies with this study:

1. The cosmological parameters were fixed to values that best fit the CMB, but slightly varying them while remaining consistent allows for a much improved fit to the BAO.
2. The CMB perceived by an average observer at the present epoch must be slightly hotter than that measured at Earth if we live on a potential hill (Section 5.3.3 of [73]). Those authors argued that slight changes to the cosmological parameters should allow a good CMB fit to be preserved, but these changes were not taken into account when predicting the BAO.
3. Related to the above, r_d would be slightly lower with a hotter CMB because we generally expect the physical size of the BAO ruler to remain about the same—but a hotter CMB implies less expansion since decoupling. Combined with the reduced H_0 that a hotter CMB requires [77], there would be a reduction in the $H_0 r_\mathrm{d}$ product, which is crucial in BAO studies.

To test the local void model at high redshift, we discuss how it affects high-z observables in Section 2, where we also describe the observational constraints. Our results are presented in Section 3 and discussed in Section 4. We conclude this paper in Section 5. Appendix A provides useful fitting formulae for the recombination and decoupling temperatures in ΛCDM as a function of the baryon and CDM densities. Appendix B discusses the evolution of the neutrino density, while Appendix C discusses the accuracy of the compressed CMB likelihood approach for handling CMB constraints on models with standard physics prior to recombination.

2. Methods and Observational Constraints

In this contribution, we focus on testing the local void model at high redshift because this greatly simplifies the setup. In general, a local void distorts the distance–redshift relation by creating additional non-cosmological contributions to the redshift through peculiar velocity and GR. Equation (52) of [73] shows that the observed redshift (z) satisfies

$$1+z = \frac{1}{a(t)} \overbrace{\sqrt{\frac{c+v_\mathrm{int}}{c-v_\mathrm{int}}}}^{\text{Doppler}} \overbrace{\exp\left(\frac{1}{c^2}\int g_\mathrm{void}\mathrm{d}r\right)}^{\text{GR}}, \tag{2}$$

where a is the cosmic scale factor at the emission time (t) of an observed photon; g_void is the outward gravitational field induced by the void due to it having less density than the cosmic mean; and v_int is the outflow velocity in the reference frame of the void, which may be moving as a whole.

A local void would have little physical effect on the high-redshift Universe. This allows us to greatly simplify the effect of a local void by neglecting peculiar velocity. Moreover, since GR would mostly arise at rather small distances, we can assume that the GR contribution remains fixed as we observe sources at ever larger redshift. We discuss the validity of

these approximations in Section 2.1. With these simplifications, the relation between the observed redshift (z) and the cosmological redshift ($z_c \equiv a^{-1} - 1$) becomes

$$1 + z \;=\; (1 + z_c)(1 + z_0), \tag{3}$$

where z_0 is a model parameter capturing the dimensionless height of the local gravitational potential hill created by the void. For a void that can solve the Hubble tension jointly with galaxy number counts, we expect that $z_0 = 0.84\%$ (Section 5.3.3 of [73]). Our main goal is to freely vary z_0, then check if its inferred value is consistent with this estimate, which was made prior to DESI without considering BAO data. We also fix z_0 to the prediction of [73] and assess the impact on the considered datasets. Since it is quite possible that somewhat different void profiles can also fit the available observations, we then consider a reduced value of $z_0 = 0.5\%$. Finally, we perform control ΛCDM analyses by setting $z_0 = 0$.

In the following sections, we discuss the validity of the z_0 approximation for the impact of a local void (Section 2.1). We then describe how z_0 affects cosmological observables at various epochs, assuming a standard background expansion history, which we briefly recap in Section 2.2. The main impact at low redshift is that the cosmological redshift is slightly smaller than the observed redshift (Sections 2.3 and 2.4). In the early Universe, the z_0 term has important implications for our interpretation of the CMB anisotropies (Section 2.5) and the sound horizon at recombination and decoupling, changing the calibration of CMB and BAO observations, respectively (Section 2.6).

2.1. Validity of the z_0 Approximation

Our approximate treatment of the impact of a local void (Equation (3)) is only expected to be valid at sufficiently high redshift. To estimate where our z_0 approximation first becomes accurate, we use Figure 1 to reproduce Figure 4 of Banik and Kalaitzidis [52]. This shows the $\alpha_{\rm iso}$ ratio between D_V/r_d and its predicted value in the ΛCDM model calibrated using *Planck* observations of the CMB [10], where D_V is the isotropically averaged BAO distance (Equation (10)). Unlike in the present study, uncertainties in cosmological parameters due to uncertainties in CMB observations were included only by means of a 0.2% error margin in r_d. This does not account for uncertainty in the predicted expansion history at low redshift, which inflates uncertainties from the CMB due to the need to extrapolate forward over many Gyr and >3 orders of magnitude in a.

The important aspect of Figure 1 for our purposes is the comparison between the thin solid and dashed lines in the same colour, with different colours indicating different initial underdensity profiles. The solid lines show model predictions including both non-cosmological sources of redshift in Equation (2), while the dashed lines show predictions considering only the special relativistic Doppler effect, excluding the impact of GR. The similarity of the predictions with and without GR shows that at low redshift, the dominant source of non-cosmological redshift is predicted to be the Doppler effect. The reason is that sources here are at a potential height similar to that of the void centre, but the gravitational fields are still able to create some outflow, which is necessary to solve the Hubble tension. The opposite occurs at high redshift, where outflows alone only negligibly distort the ΛCDM prediction. This is apparent from the dashed lines without GR lying almost on top of the ΛCDM expectation ($\alpha_{\rm iso} = 1$). However, the solid lines including GR are still appreciably different from ΛCDM. It is therefore clear that GR is the dominant source of non-cosmological redshift at high redshift. This is because sources very far out are not directly affected by outflow from a local void. Its only impact is an observational effect due to the need for photons from such sources to climb the local gravitational potential hill in order to reach our detectors.

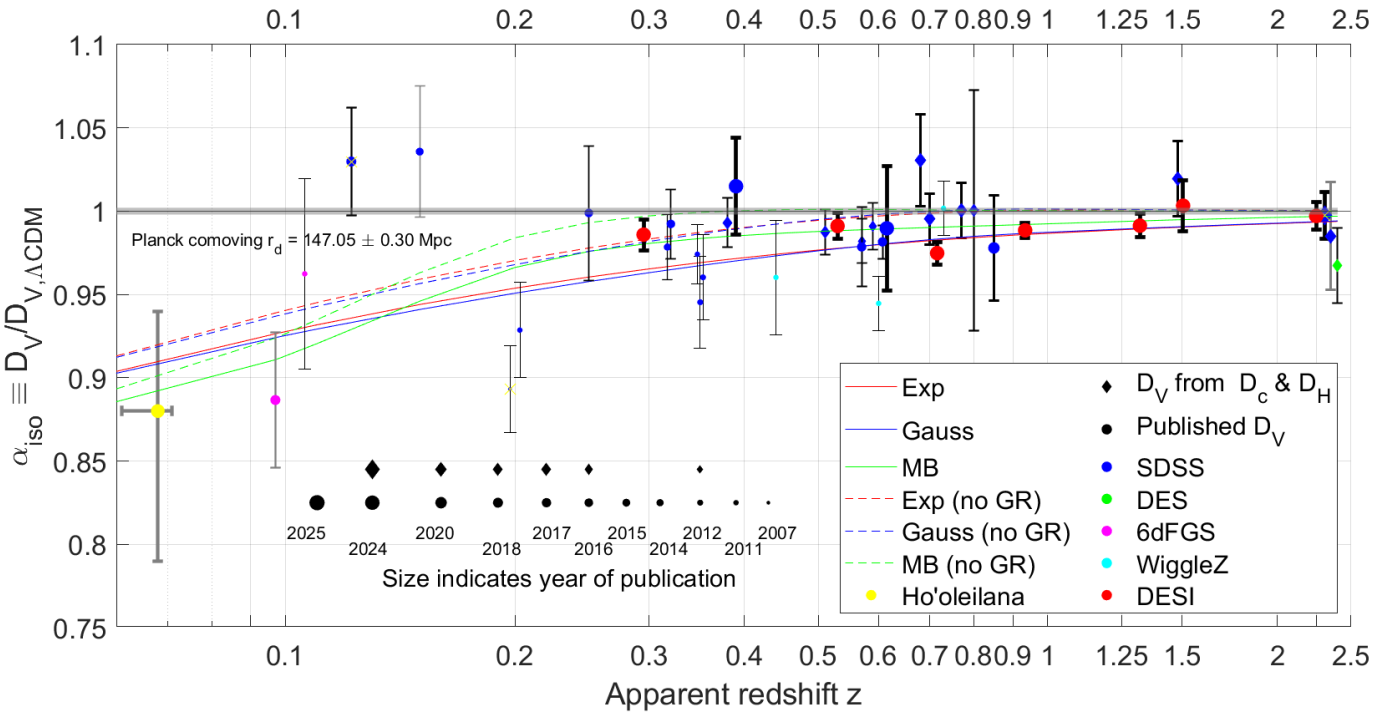


Figure 1. Ratio between the isotropically averaged BAO distance scale (D_V) and the ΛCDM prediction based on *Planck* observations of the CMB [10]. The shaded grey horizontal band shows a 0.2% uncertainty on the ΛCDM prediction due to the *Planck* uncertainty on r_d [10], though this does not properly account for the uncertainties (see the text). The coloured lines show predictions of the best-fitting void models from [73] with an initial underdensity profile that is exponential (red), Gaussian (blue), or Maxwell–Boltzmann (green). Solid lines show predictions including both non-cosmological redshift contributions in Equation (2), while the dashed lines in the same colour show the corresponding results without the GR contribution. This highlights that the dominant non-cosmological contribution is the Doppler effect at low redshift, while GR dominates at high redshift. Points with uncertainties show BAO measurements over the last 20 years, with different colours indicating different surveys and larger markers indicating more recent results, as indicated towards the bottom left. Reproduced from Figure 4 of Banik and Kalaitzidis [52].

Figure 1 shows that GR is more important than the Doppler effect at $z \gtrsim 0.3$ for all three density profiles considered in [73]. We therefore consider data from a 'nominal redshift range' of $z > 0.5$, where GR completely dominates over the Doppler effect of outflow velocities. This allows us to address 12 of the 13 BAO measurements from DESI DR2 [50]. We complement this by considering an 'extended redshift range' of $z > 0.29$ for most analyses. This simplifies the comparison with other studies that typically include all 13 BAO measurements. We argue that the z_0 approximation should still work fairly well at this lower redshift because GR is still dominant over the Doppler effect at $z \gtrsim 0.3$. Sources at $z = 0.29 - 0.5$ would be partway up the local potential hill, reducing the GR contribution compared to that for a very distant source. On the other hand, outflows are obviously important at $z \approx 0.3$ in the local void model. These would increase the non-cosmological redshift via the Doppler effect (Equation (2)). We can suppose that there would be an approximate cancellation between the impact of a reduced GR contribution and an unmodelled outflow contribution to z. The results for our extended redshift range should clearly be taken with some caution, given the approximate nature of this argument, but we note that the z_0 approximation would become valid at lower redshift with a smaller void than that proposed in [73], as suggested based on peculiar velocities [78]. This would make the z_0 approximation more accurate at the redshifts considered here. Bearing these caveats in mind, we show variants of most of our analyses in which we consider data at

$z > 0.29$. The extra data from $z = 0.29 - 0.5$ tightens the constraints somewhat compared to our nominal analysis.

2.2. Friedmann Equation with Neutrinos

By construction, the local void model does not alter the standard $a(t)$. Considering dark energy, matter, radiation, and neutrinos, the Friedmann equation for $E \equiv H/H_0$ is expressed as follows [53]:

$$E^2(a) = \Omega_\Lambda + \frac{\Omega_{\rm bc}}{a^3} + \frac{\Omega_\gamma}{a^4} + \frac{\Omega_{\nu,{\rm ur},i}}{a^4}\left[1 + \sum_{i=A,B}\sqrt{1 + \left(\frac{a}{a_{{\rm nr},i}}\right)^2}\right], \tag{4}$$

where Ω_x refers to the present fraction of the cosmic critical density ($3H_0^2/(8\pi G)$) in component x (which is Λ, bc, γ, or ν for dark energy, baryons + CDM, photons, or neutrinos, respectively) and $\Omega_{\nu,{\rm ur},i}$ is the present contribution of each neutrino species (i) if these neutrinos were massless, while $a_{{\rm nr},i}$ is the scale factor when they transition from ultra-relativistic to non-relativistic. We label the neutrino species as A, B, and C in descending order of rest mass. The final term only includes species A and B due to our assumption that neutrinos of species C are massless, therefore behaving like radiation. For the massive species (A and B), we find $a_{\rm nr,i}$ using the approach discussed in Appendix B, which also recaps the ratio between photon and neutrino energy densities in the ultra-relativistic limit. We follow the same outline as Appendix B of [53], but unlike their study, we assume different masses for the different neutrino species to better conform to terrestrial neutrino experiments. We follow the usual convention of keeping the neutrino masses as low as possible, so the neutrino species are assumed to have $m_{\nu,i} = (50, 10, 0)$ meV$/c^2$. This places the transition from relativistic to non-relativistic behaviour at $z \approx 100$ (20) for species A (B), while species C is massless. The matter density parameter ($\Omega_{\rm m}$) applicable to lower redshift datasets includes the massive neutrino contribution (Equation (22)). The photon energy density follows from standard blackbody physics assuming a photon temperature of $T_{\rm CMB}$ (Equation (11)). Motivated by inflationary theory, we only consider flat models, neglecting the curvature contribution.

2.3. Cosmic Chronometers (CCs)

The stellar populations in passively evolving galaxies serve as excellent CCs [42,43,79–82]. The relative age between galaxies at different redshifts constrains the expansion history even more directly than the distance–redshift relation, since there is no need to convert distances into lookback times through division by c. Observers report CC results in the form of

$$H_{\rm CC}(z) \;=\; -\frac{\dot{z}}{1+z}\,, \tag{5}$$

which is generally not the same as $H(z)$. Assuming a fixed GR contribution to the redshift, applying the chain rule to Equation (3) tells us that

$$\mathrm{d}z \;=\; (1+z_0)\mathrm{d}z_{\rm c}\,. \tag{6}$$

This inflates both $\dot{z}$ and $(1+z)$ by the same factor of $(1+z_0)$, which therefore cancels out. Taking into account that observations at a redshift of z are actually probing the apparent expansion rate at the cosmological redshift ($z_{\rm c} < z$), Equation (5) reduces to

$$H_{\rm CC}(z) \;=\; H(z_{\rm c}). \tag{7}$$

We compare predictions for $H_{\rm CC}(z)$ with a widely used compilation of 32 observations [81] supplemented by a very recent measurement at $z = 0.12$ [83]. However, not all 33 of these CC measurements are used in our analyses because the z_0 model is not a valid approximation of a local void at low redshift (Section 2.1). This requires us to consider only those CC measurements beyond the redshift floor imposed for each analysis (0.29 or 0.5).

2.4. Comoving and Hubble Distances from BAO

The BAO signal provides both a redshift depth and an angular scale [52]. Equation (6) shows that the redshift depth is inflated by a factor of $(1 + z_0)$, reducing the inferred Hubble distance ($D_H \equiv c/H$).

$$D_H(z) \;=\; \frac{D_H(z_{\rm c})}{1+z_0}\,. \tag{8}$$

The angular BAO scale is used to constrain the comoving distance ($D_{\rm c}$) to the redshift of the used tracer, where

$$D_{\rm c} \;\equiv\; c\int_0^{z_{\rm c}} \frac{d\tilde{z}_c}{H(\tilde{z}_c)}\,. \tag{9}$$

This remains true in the z_0 model, provided we calculate the $D_{\rm c}$ integral in terms of $z_{\rm c}$ rather than z. This is because the BAO constraint on $D_{\rm c}$ tells us the comoving distance to $z_{\rm c}$ in the void-free cosmology, implying that $H(z_{\rm c})$ must be used in the integral rather than $H(z)$.

We use the 13 BAO measurements from DESI DR2 [50]. In our nominal analysis considering only data at $z > 0.5$, we neglect the lowest redshift measurement of $D_{\rm V}/r_{\rm d}$, where $D_{\rm V}$ is the isotropically averaged BAO distance.

$$D_{\rm V}(z) \;\equiv\; \Big[z D_{\rm c}^2(z) D_H(z)\Big]^{1/3}. \tag{10}$$

The other measurements tell us $(D_{\rm c}/r_{\rm d}, D_H/r_{\rm d})$ and their covariance at six redshifts, leading to a total of $1 + 6 \times 2 = 13$ measurements and a block-diagonal covariance matrix. In our extended analyses using data at $z > 0.29$, we consider all 13 measurements. Since BAO measurements must be calibrated using some assumed $r_{\rm d}$, we recalculate it at each step of our analysis using the approach described in Section 2.6.

2.5. CMB Temperature and Anisotropies

The GR contribution in Equation (2) would also affect CMB photons. This would make the CMB appear to be slightly cooler than it actually is. In other words, an idealised observer at the present epoch (not on a potential hill or in a potential well) would measure a CMB temperature of

$$T_{\rm CMB} \;=\; T_{\rm FIRAS}(1+z_0), \tag{11}$$

where $T_{\rm FIRAS} = 2.72548 \pm 0.00057$ K is the temperature observed by the Far-Infrared Absolute Spectrophotometer (FIRAS) instrument onboard the *Cosmic Background Explorer* (*COBE*) satellite [84]. We neglect the negligible uncertainty on $T_{\rm FIRAS}$.

The impact of a hotter CMB has been explored in a few previous studies [77,85]. The main impact is that since the recombination temperature ($T_\star$) is almost fixed, there must have been less expansion since recombination. To preserve the physics in the primordial Universe, the present baryon and matter densities must be correspondingly increased.

Therefore, the standard CMB constraint on the physical baryon density (w_b) must be reinterpreted as a constraint on

$$\widetilde{w}_\mathrm{b} \equiv \frac{w_\mathrm{b}}{(1+z_0)^3}, \tag{12}$$

where $h \equiv H_0$ in units of 100 km/s/Mpc, $w_x \equiv \Omega_x h^2$ for any component (x), and the tilde denotes division by $(1+z_0)^3$. This argument also applies to $w_\mathrm{bc} \equiv w_\mathrm{b} + w_\mathrm{c}$, the total matter contribution at early times. To match the constraint on the angular scale of the acoustic peaks, a slightly lower H_0 is required for a hotter CMB [77]. Those authors showed that with these changes, the primary CMB anisotropies are unaltered because the physics in the early Universe and the comoving distance to recombination remain the same. This means the CMB power spectrum is barely affected. There is a subtle effect on large angular scales, which we return to in Section 4.1.

Since a core objective of the local void model is to avoid introducing new physics at early times, we can follow standard techniques when comparing the void model to the CMB. We do this using the compressed CMB likelihood [86], a widely used approximation that preserves most of the information contained in the full CMB likelihood [50]. We demonstrate the accuracy of this framework in Appendix C. Within this framework, the CMB constraints are expressed in terms of the parameter vector $(100\,\theta_\star, w_\mathrm{b}, w_\mathrm{bc})$, where

$$\theta_\star = \frac{r_\star}{D_\mathrm{c}(a_\star)}, \tag{13}$$

where r denotes the comoving sound horizon and $\star$ subscripts denote recombination. The comoving distance to it is found using Equation (4) for $H(z)$, while the sound horizon is found using Equation (15).

We obtain our adopted CMB constraints on $(100\,\theta_\star, \widetilde{w}_\mathrm{b}, \widetilde{w}_\mathrm{bc})$ from the chains in [12], which combines *Planck* 2020 [10], SPT-3G [12], and ACT DR6 [11]. The observed values of these parameters and their associated covariance matrix are expressed as follows:

$$\begin{aligned} \mu_\mathrm{obs}(100\,\theta_\star, \widetilde{w}_\mathrm{b}, \widetilde{w}_\mathrm{bc})^\mathrm{T} &= (1.04161,\ 0.02240,\ 0.14265), \\ \mathbf{C}_\mathrm{CMB} &= 10^{-9} \times \begin{bmatrix} 53.8482 & 1.10723 & -28.7005 \\ 1.10723 & 9.20447 & -17.6016 \\ -28.7005 & -17.6016 & 843.132 \end{bmatrix}. \end{aligned} \tag{14}$$

These are slightly updated from the results stated in Appendix B of [53] because that referenced an older version of SPT-3G Collaboration [12], but here, we use its final published version in which the authors corrected a previous coding error.

A higher matter density necessarily implies a higher $H(a)$ in the matter-dominated era. To compensate for and preserve $D_\mathrm{c}(a_\star)$, we must reduce $H(a)$ at late times. This is possible through a reduced dark energy density. We therefore expect a hotter CMB to be associated with reduced H_0 [77]. However, we find that the H_0 shift is quite small compared to uncertainties in the local cz'. A more serious issue is that the reduced H_0 reinforces the reduced r_d (Section 2.6) to yield a smaller $H_0 r_\mathrm{d}$ product, which is tightly constrained by BAO.

2.6. CMB and BAO Sound Horizons

One of the most precisely constrained quantities in cosmology is $\theta_\star$, the ratio between the comoving distance to recombination and the comoving sound horizon at that epoch. We compute $r_\star$ using the exact analytic result from [8]:

$$r_\star = \frac{2c}{3}\sqrt{\frac{3\,a_{\rm eq}}{\Omega_{\rm bc}H_0^2\mathcal{R}_{\rm eq}}}\ln\left(\frac{\sqrt{1+\mathcal{R}_\star}+\sqrt{\mathcal{R}_\star+\mathcal{R}_{\rm eq}}}{1+\sqrt{\mathcal{R}_{\rm eq}}}\right), \tag{15}$$

where $\star$ subscripts denote recombination; eq subscripts denote matter–radiation equality (treating neutrinos as radiation; Equation (A6)); bc refers to the combination of baryons and CDM; and $\mathcal{R} \equiv 3\rho_{\rm b}/(4\rho_\gamma)$ is related to the speed of sound, which depends on the ratio between the baryon density ($\rho_{\rm b}$) and the photon density (ρ_γ) (see Appendix B of [53]).

To solve Equation (15), we need to know $\mathcal{R}_\star$ and, thus, the recombination scale factor ($a_\star$). We do not obtain this following the approach of [53], as it relies on an ancient fitting formula, albeit rescaled to better line up with modern results. Instead, we run the Cosmic Linear Anisotropy Solving System (CLASS; [87]) over a small grid of parameters centred approximately where we expect the posterior inference to peak based on preliminary calculations. For reasons described in Section 2.5, we set up our grid in terms of the parameters $\widetilde{w}_{\rm b}$, $\widetilde{w}_{\rm bc}$, and z_0. For each step in our grid, we record the recombination temperature ($T_\star$), which should reduce the sensitivity to z_0. We also record the decoupling temperature ($T_{\rm d}$), which corresponds to the end of the 'drag epoch' when photons have significant momentum exchange with baryons. We use d subscripts to denote quantities evaluated at this epoch, when the BAO $r_{\rm d}$ becomes fixed.

We obtain $a_\star$ from $T_\star$ using the following relation:

$$a_\star = \frac{T_{\rm CMB}}{T_\star}, \tag{16}$$

where $T_{\rm CMB}$ is found using Equation (11). There is an analogous relation between $a_{\rm d}$ and $T_{\rm d}$, which is important for the BAO. We find $r_{\rm d}$ by applying Equation (15) using $\mathcal{R}_{\rm d}$ instead of $\mathcal{R}_\star$. We note that this equation cannot be applied at any later stage in cosmic history because it assumes tight coupling between photons and baryons.

Since $T_\star$ and $T_{\rm d}$ do not change much across our parameter grid, we approximate these temperatures as depending quadratically on the model parameters. Thus, we assume that

$$T_\star = T_\star^{\rm ref} + \boldsymbol{d}^{\rm T}\boldsymbol{g}_\star + \frac{\boldsymbol{d}^{\rm T}\mathbf{H}_\star\boldsymbol{d}}{2}, \tag{17}$$

where $T_\star^{\rm ref} = 2970.24$ K, $\boldsymbol{d} \equiv \Theta - \Theta_{\rm ref}$ is the difference between the model parameters and the reference values at the grid centre, $\boldsymbol{g}_\star$ is the gradient of $T_\star$ with respect to the considered parameters, and $\mathbf{H}_\star$ is the Hessian. $T_{\rm d}$ is found using an analogous procedure. The grid we use is centred on

$$\Theta_{\rm ref} \equiv \begin{pmatrix}\widetilde{w}_{\rm b}\\ \widetilde{w}_{\rm bc}\\ z_0\end{pmatrix}_{\rm ref} = \begin{pmatrix}0.0225\\ 0.1450\\ 0.0100\end{pmatrix}. \tag{18}$$

Using our CLASS grid, we find that

$$\boldsymbol{g}_\star = \begin{pmatrix}-3187.35\\ 194.00\\ -3.90\end{pmatrix}, \quad \mathbf{H}_\star = \begin{bmatrix}265184.96 & -7854.34 & 144.61\\ -7854.34 & -491.81 & -9.32\\ 144.61 & -9.32 & 23.46\end{bmatrix}. \tag{19}$$

Across our parameter grid, the maximum absolute error in $T_\star$ is only 1.1 mK, while the root mean square (rms) error is only 0.24 mK. Given that $T_\star \approx 2970$ K, our quadratic approximation to $T_\star$ is more than sufficient for our purposes.

We obtain T_d similarly to Equation (17). Since we extract both $T_\star$ and T_d from CLASS when running it, Θ_ref remains the same as in Equation (18). The reference temperature is now only $T_\mathrm{d}^\mathrm{ref} = 2892.72$ K, while the gradient and Hessian become

$$\boldsymbol{g}_\mathrm{d} = \begin{pmatrix} 5926.80 \\ 203.29 \\ -2.37 \end{pmatrix}, \quad \mathbf{H}_\mathrm{d} = \begin{bmatrix} -189596.68 & -4765.72 & 108.90 \\ -4765.72 & -624.69 & -5.34 \\ 108.90 & -5.34 & 17.11 \end{bmatrix}. \tag{20}$$

The maximum absolute error in T_d across our parameter grid is only 1.0 mK, while the rms error is only 0.34 mK. This is, again, a negligibly small fraction of $T_\mathrm{d} \approx 2890$ K.

We expect that $T_\mathrm{d} < T_\star$ because the recombination redshift is defined as the maximum of the visibility function, which, roughly speaking, requires photons to be unaffected by baryons. Since there are far fewer baryons than photons, this is relatively easy to obtain, so it occurs earlier in cosmic history. However, decoupling requires baryons to no longer be 'dragged' by photons. Since there are far more photons than baryons, the ionisation fraction has to drop far lower to reach this stage. Therefore, baryon–photon decoupling occurs later in cosmic history than recombination.

2.7. BBN

In the first few minutes after the Big Bang, the whole Universe was hot enough to fuse hydrogen nuclei into deuterium and helium, along with trace amounts of metals [88–91]. The precise details of BBN have a large impact on the final yields of non-trivial nuclei, making their measured primordial abundances a sensitive probe of the baryon:photon ratio (η).

Since BBN provides a tight constraint on η, studies that report a BBN constraint on w_b must assume some value for the present photon temperature. This is presumably T_FIRAS, which, nowadays, is typically assumed without question. We therefore assume that any reported BBN constraints on w_b are actually constraints on $\widetilde{w}_\mathrm{b}$. Since the CMB also constrains $\widetilde{w}_\mathrm{b}$ (Section 2.5), a slightly hotter CMB would not affect the agreement in standard theory between w_b inferred from BBN and that from the CMB anisotropies [90].

Applying the PRIMAT nuclear reaction code [92] to BBN, assuming a primordial deuterium abundance of $(D/H)_\mathrm{p} = (2.527 \pm 0.030) \times 10^{-5}$ [93] and a primordial helium abundance of $Y_\mathrm{p} = 0.2449 \pm 0.004$ [94], the baryon density is $\widetilde{w}_\mathrm{b} = 0.021915 \pm 0.000215$ [95]. This result is based on the purely BBN section of their Table B1 with a fixed N_eff, corresponding to the effective number of neutrino species. For simplicity, we symmetrised their very slightly asymmetric error bars while fixing their reported 1σ lower and upper limits on $\widetilde{w}_\mathrm{b}$. We adopt this constraint on $\widetilde{w}_\mathrm{b}$ by adding the corresponding χ^2 contribution.

3. Analysis and Results

We conduct several analyses to understand the impact of z_0. The most obvious is to let z_0 be a free parameter, which we infer. Since we have a clear *a priori* expectation that $z_0 \approx 0.84\%$ (Section 5.3.3 of [73]), we also run analyses where we fix z_0 to 0.84%. Given the results of Stiskalek et al. [78] suggesting a smaller void, we also consider the case of $z_0 = 0.5\%$. ΛCDM behaviour is recovered by fixing $z_0 = 0$. We also extend our main analysis by including SNe Ia from the recent Dark Energy Survey (DES) Dovekie catalogue [96,97]. The prior ranges of the model parameters are summarised in Table 1.

Table 1. The range for the uniform prior we adopt on each model parameter.

Parameter	Prior Range
w_b	(0.02, 0.025)
w_bc	(0, 0.5)
H_0 (km/s/Mpc)	(50, 90)
z_0	$(-0.1, 0.1)$

3.1. Nested Sampling of Model Parameters

We use the `dynesty`[1] nested sampling algorithm [98–102] to compute the posterior probability and the Bayesian evidence (Z), given by

$$Z(\mathcal{M}) = \int P(\theta)\, P(\mathbf{D}|\theta, \mathcal{M}) \mathrm{d}\theta, \tag{21}$$

where θ is the parameter vector, $P(\theta)$ is the prior, and $P(\mathbf{D}|\theta, \mathcal{M})$ is the likelihood of data $\mathbf{D}$ given model $\mathcal{M}$ with parameters of θ. We take 500 live points and use a stopping criterion of $\Delta \ln \hat{Z} = 0.01$, where the hat denotes that this is the approximate remaining Z, not the true Z. We will see later that this tolerance is sufficient because the different models considered herein have much larger differences in Z. We plot the 1σ and 2σ contours using the `GetDist` package[2] [103]. Posterior convergence was confirmed by checking that the number of effective samples was $N_\mathrm{eff} > 2000$ for all analyses.

Our full nested sampling analyses consider the parameters w_b, w_bc, H_0, and z_0. We do not infer Ω_m; rather, we compute it by adding the baryon + CDM contribution to that of the neutrinos which are non-relativistic at low redshift.

$$w_\mathrm{m} = w_\mathrm{bc} + \sum_{i=A,B} w_{\nu,i}\,. \tag{22}$$

Late-time observables like BAO and CC are sensitive to Ω_m, while early-Universe observables like the CMB are sensitive to Ω_bc, as the neutrinos are still relativistic then.

Figure 2 shows the triangle plot resulting from our full analysis, with open black contours showing our nominal redshift range and filled red contours showing our extended redshift range. The previously published expectation that $z_0 = 0.84\%$ is shown as a dotted line in panels involving z_0. It is clear that the posterior inference on z_0 is consistent with 0.84%, though it peaks at a very slightly negative z_0. Using the extended redshift range reduces the uncertainties, but interestingly, the inferred z_0 rises slightly, so the mild tension with the predicted 0.84% remains about the same. This is because the DESI DR2 measurement of $D_\mathrm{V}/r_\mathrm{d}$ at $z = 0.295$ lines up better with the void model, as we discuss later (Section 3.2).

The degeneracies apparent in Figure 2 are to be expected from previous analyses. For instance, we expect a negative correlation between Ω_m and h due to the shape of the CMB power spectrum providing a tight constraint on w_m and the opposite impacts of Ω_m and h on $\theta_\star$ [104,105]. As discussed in Section 2.5, we also expect a negative correlation between z_0 and h because a hotter CMB implies a higher matter density and, thus, a higher expansion rate at high redshift, which must be compensated for by a lower expansion rate at low redshift to maintain the same comoving distance to recombination (see also [77]). These degeneracies are, indeed, apparent from our results, explaining the induced positive correlation between z_0 and Ω_m.

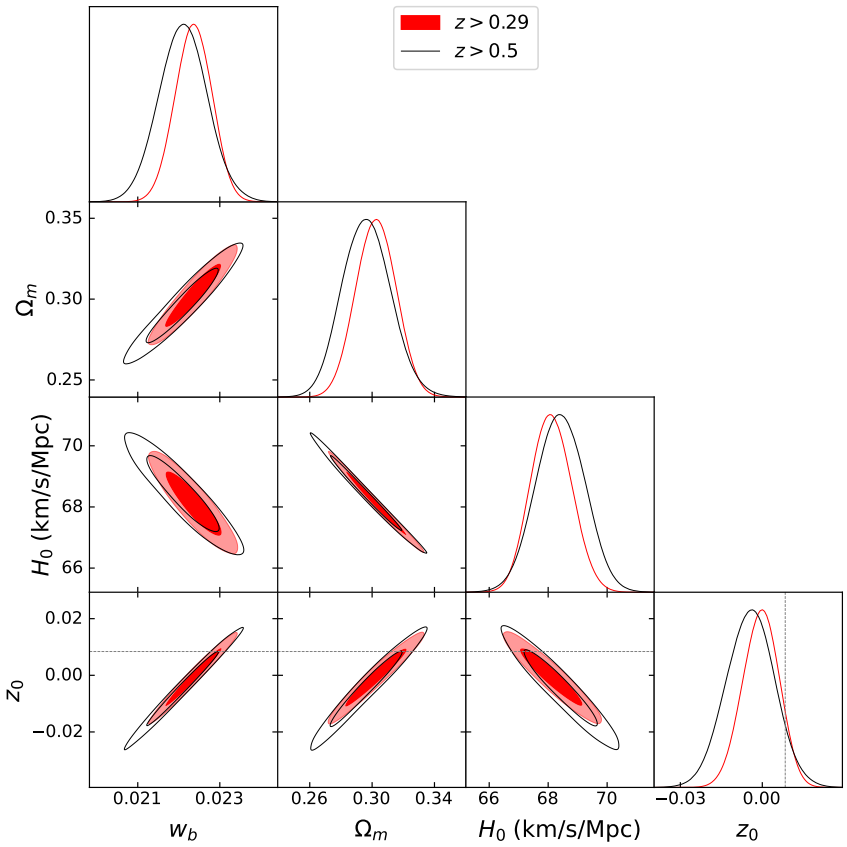


Figure 2. Triangle plot showing the inferred parameters with data from $z > 0.5$ (open black contours) or $z > 0.29$ (filled red contours). We show the 1σ and 2σ error ellipses in panels involving two parameters. The dotted line shows the *a priori* prediction that $z_0 = 0.84\%$ (Section 5.3.3 of [73]).

The inferred model parameters are summarised in Table 2. The reported central value is the mean across the `dynesty` chain, while the 1σ confidence interval is taken to be the range between percentiles 15.87 and 84.13. The first column shows results with free z_0, while other columns show results with z_0 fixed to 0 (ΛCDM), 0.5%, or 0.84%. Fixing z_0 reduces the uncertainties considerably, but it also slightly shifts the inferred values due to the parameter degeneracies discussed above. The inferred z_0 is slightly negative with our nominal redshift range, but it is almost exactly 0 with our extended redshift range. In both cases, the prediction of 0.84% [73] is just outside the 1σ range.

Table 2. Inferred parameter values under different assumed z_0 scenarios for the nominal redshift range (top) and extended redshift range (bottom).

		Assumed Value of z_0		
Parameter	**Free z_0**	**0 (ΛCDM)**	**0.005**	**0.0084**
		$z > 0.5$ dataset		
w_b	$0.02211^{+0.00057}_{-0.00059}$	0.02239 ± 0.00008	0.02273 ± 0.00009	0.02295 ± 0.00008
Ω_m	0.296 ± 0.015	0.303 ± 0.003	0.313 ± 0.004	0.319 ± 0.004
H_0 (km/s/Mpc)	$68.42^{+0.83}_{-0.82}$	68.04 ± 0.26	67.59 ± 0.25	$67.29^{+0.26}_{-0.24}$
z_0	$-0.004^{+0.008}_{-0.009}$	–	–	–
		$z > 0.29$ dataset		
w_b	$0.02236^{+0.00046}_{-0.00044}$	0.02239 ± 0.00008	0.02272 ± 0.00009	0.02295 ± 0.00009
Ω_m	0.303 ± 0.013	0.303 ± 0.003	0.313 ± 0.003	0.319 ± 0.004
H_0 (km/s/Mpc)	68.11 ± 0.69	68.07 ± 0.23	$67.58^{+0.24}_{-0.24}$	$67.25^{+0.26}_{-0.23}$
z_0	-0.001 ± 0.007	–	–	–

3.2. Reconstructed BAO Distance Scale

To gain further insight into the impact of z_0 on BAO predictions, we use our `dynesty` chain to obtain the posterior predictive distribution (PPD) of D_V/r_d at each redshift in the range of (0.1, 2.5). This allows us to obtain the mean value of D_V/r_d and its 1σ confidence interval, which we, again, approximate using percentiles 15.87–84.13. For the 2σ confidence interval, we use percentiles 2.275–97.725.

Since D_V/r_d spans a large range in values over such a wide redshift range, it is common to divide D_V/r_d at each redshift by the value in some fiducial cosmology. For this, we use the mean value of the PPD of D_V/r_d in the ΛCDM model ($z_0 = 0$). This approach is similar to using the best-fitting ΛCDM model as our fiducial cosmology when calculating α_{iso}, which is defined as D_V/r_d divided by the fiducial value. However, our approach involves obtaining D_V/r_d from a fiducial framework (ΛCDM) instead of a fiducial model (ΛCDM with best-fitting values of its parameters). We note that the fiducial D_V/r_d has no bearing on our statistical results, as it is used only for plotting purposes. We will see that using a fiducial ΛCDM cosmology with parameters that best fit all considered high-redshift datasets leads to important differences compared to considering just the CMB (Figure 1).

Figure 3 shows our reconstructed $\alpha_{iso}(z)$ using our analysis with free z_0. The solid blue line shows the mean of the PPD on D_V/r_d at each z, while the dark- and light-blue bands show the 1σ and 2σ confidence intervals, respectively. The DESI data points are shown in red. Since the ΛCDM model is used as the fiducial cosmology, the ΛCDM prediction is, by definition, $\alpha_{iso} = 1$, which we highlight as a dotted grey line. This fits most of the data points quite well, underscoring the lack of a clear BAO anomaly in ΛCDM when considering only high-redshift datasets. Although a BAO anomaly is widely discussed in the literature [50] and often attributed to evolution of the dark energy density in a theoretically problematic manner [106], the anomaly is not apparent in the DESI data space [53]. It is apparent in the commonly used $(H_0 r_d, \Omega_m)$ parameter space, an issue we return to later (Section 3.3).

A crucial aspect of Figure 3 is the prediction of the best-fitting model where z_0 is fixed to various values. The predicted run of α_{iso} for the 0.5% case is shown using the solid green curve, while the solid black curve shows results with z_0 fixed to the previously expected 0.84% [73]. In both cases, the results are in good agreement with the reconstructed $\alpha_{iso}(z)$ when assuming a free z_0. There is a slight mismatch with DESI DR2 at $z = 0.7$ and 0.9, but this is also the case for ΛCDM. Raising z_0 to 0.5% or even 0.84% only slightly worsens the tension here.

The minimum χ^2 of each considered model is shown in Table 3. The parameters are usually optimised to minimise χ^2 with a fixed z_0, but in the central column, z_0 is also varied, and its best-fitting value is indicated. Each row shows the contribution to the total χ^2 from each considered observable, for which we give the number of degrees of freedom (d.o.f.). All χ^2 contributions and the total are clearly acceptable for ΛCDM, as might be expected from Figure 3 and the low data-space BAO–CMB tension [53]. Unlike the Hubble tension in which the CMB and local cz' cannot be fit simultaneously, we can adequately fit the CMB and BAO datasets in ΛCDM. However, the parameters required for this are clearly not exactly the same as those that best fit the CMB. Indeed, fixing the parameters to those in the *Planck* cosmology [10] leads to almost 3σ tension with DESI DR2 [52]. This shows the continued importance of improving CMB constraints to better assess the BAO anomaly [12].

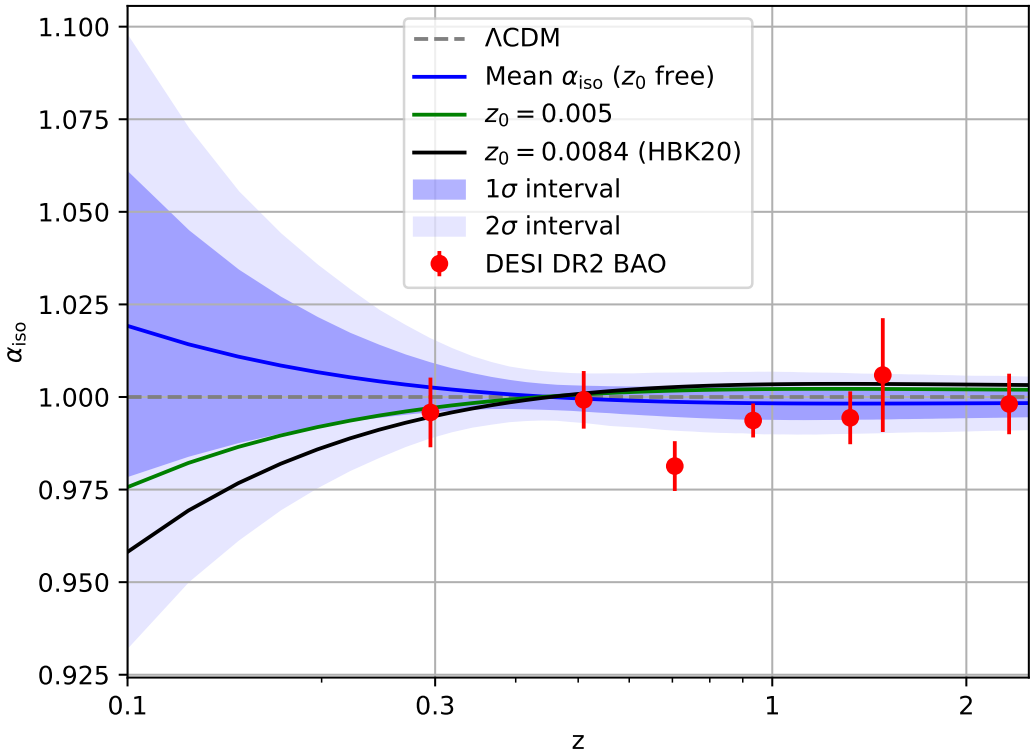


Figure 3. Reconstructed $\alpha_{\rm iso}(z) \equiv D_{\rm V}/r_{\rm d}$ in units of its fiducial value at each redshift, which, here, is the mean value from our ΛCDM nested sampling analysis using data at $z > 0.5$ (see the text). The solid blue line shows the mean result using our free z_0 analysis with the same data, while the shaded blue bands show the 1σ and 2σ uncertainties using Gaussian equivalent percentiles. The red data points with uncertainties show DESI DR2 measurements [50]. The solid green line shows the best-fitting model with $z_0 = 0.5\%$, while the solid black line assumes the previously expected value of $z_0 = 0.84\%$ [73].

Table 3. The χ^2 contributions from each considered observable and the total for each assumed z_0 scenario, shown here considering data in our nominal redshift range (top) and extended redshift range (bottom). The numbers in brackets in the first column show how many d.o.f. each observable contributes.

Observable (d.o.f.)	**Assumed Value of z_0**			
	0 (ΛCDM)	**−0.0044 (Best)**	**0.005**	**0.0084**
		$z > 0.5$ dataset		
BBN (1)	4.855	4.919	4.782	4.733
CMB (3)	6.070	6.501	5.603	5.300
BAO (12)	15.307	14.612	16.669	17.950
CC (14)	11.561	11.514	11.625	11.675
Total (30)	37.793	37.547	38.680	39.659
		$z > 0.29$ dataset		
	0 (ΛCDM)	-5.4×10^{-4} (best)	0.005	0.0084
BBN (1)	4.905	4.921	4.764	4.668
CMB (3)	6.494	6.606	5.507	4.885
BAO (13)	14.989	14.854	16.791	18.611
CC (23)	13.417	13.418	13.429	13.458
Total (40)	39.805	39.799	40.492	41.623

As might be expected from the slightly negative inferred values of z_0, fixing it to a positive value of 0.5% or 0.84% slightly increases the total χ^2. Interestingly, this improves

the agreement with the CMB, especially for our extended redshift range. However, this is more than offset by increased χ^2 from BAO. Even so, the differences in χ^2 are rather small, especially with BBN and CC. Changes to the total χ^2 do not clearly favour any of the considered z_0 values over any other. This highlights that $z_0 = 0.84\%$ lies within present uncertainties. We can envisage that a slightly different void model with $z_0 = 0.5\%$ might also fit low-z constraints like the local cz'. This would be in even better agreement with the high-redshift datasets considered here.

3.3. Quantifying the BAO Anomaly

To quantify whether the BAO data can be predicted by a model with parameters constrained using the non-BAO datasets considered here, we follow the approach of [53]. Those authors defined two metrics known as the data-space and parameter-space tensions, the former working directly in the DESI data space (12 or 13 d.o.f.) and the latter in the $(H_0 r_\mathrm{d}, \Omega_\mathrm{m})$ parameter space (2 d.o.f.), which is commonly used in BAO analyses because these are the two main quantities which can easily be extracted. We avoid using non-standard parameter spaces to quantify the tension faced by each model, since this can create look-elsewhere effects associated with considering multiple possible metrics.

The data-space tension captures the extent to which the individual DESI measurements can be predicted by a model that has been fitted to other data. Usually, only the CMB is considered, but since there is little tension between it and CC [43] or BBN [91], we use all non-BAO datasets to constrain the parameters of each model when predicting the BAO angular scale and redshift depth. Uncertainties in both the DESI observations and model predictions must be considered when calculating the total χ^2, which is then converted into a Gaussian equivalent tension for 12 or 13 d.o.f., depending on whether we are using our nominal or extended redshift range, respectively. The parameter-space tension is calculated similarly, but this has only 2 d.o.f. Following [53], we recommend that the maximum of the data- and parameter-space (MDPS) tension be used to efficiently quantify the BAO anomaly in any model, since both contain useful information and neither should be large in the correct model. In the community, the focus is usually on the parameter-space tension, which is the MDPS tension for ΛCDM.

The top part of Table 4 shows the BAO tension in data and parameter space for our nominal redshift range. Given that models with $z_0 = 0.5\%$ or even 0.84% are barely distinguishable from ΛCDM at the level of current observations, it is unsurprising that, just as with ΛCDM, these non-standard $z_0 > 0$ scenarios have more tension in parameter space than in data space. The MDPS tension for ΛCDM is 3.01σ. Fixing z_0 to the previously expected level of 0.84% [73] reduces the MDPS tension to 2.93σ. This slightly worsens the data-space tension from 2.10σ to 2.32σ, which is quite small in both cases. There appears to be an interesting tradeoff between the tension in data and parameter space. The local void model appears able to navigate this subtlety in such a way that the MDPS tension is reduced, thereby slightly alleviating the conventional measure of the BAO anomaly.

The reduced MDPS tension in the local void model is even more apparent in the bottom part of Table 4, which shows the BAO tension for our extended redshift range. In this case, ΛCDM faces a tension of 3.07σ, but this is reduced to 2.79σ with $z_0 = 0.84\%$. Note that since z_0 is fixed in both z_0 scenarios, the parameter uncertainties are almost identical (Table 2). The reduced MDPS tension must then arise from assuming $z_0 > 0$ genuinely shifting the regions of $(H_0 r_\mathrm{d}, \Omega_\mathrm{m})$ parameter space preferred by the BAO and non-BAO datasets considered here.

Table 4. BAO tensions for our nominal redshift range (top) and extended redshift range (bottom), showing the data-space and parameter-space χ^2 and corresponding Gaussian equivalent tension for each assumed z_0 scenario. The MDPS tension is highlighted in bold in each column.

Assumed z_0	0	-0.0044	0.005	0.0084
Nominal redshift range				
Data-space χ^2 (12 d.o.f.)	22.14	22.35	22.91	24.03
Data-space tension	2.10σ	2.12σ	2.19σ	2.32σ
Parameter-space χ^2 (2 d.o.f.)	11.88	13.40	11.44	11.38
Parameter-space tension	$\mathbf{3.01\sigma}$	$\mathbf{3.23\sigma}$	$\mathbf{2.94\sigma}$	$\mathbf{2.93\sigma}$
Extended redshift range				
Assumed z_0	0	-5.4×10^{-4}	0.005	0.0084
Data-space χ^2 (13 d.o.f.)	22.31	22.22	23.18	24.56
Data-space tension	1.95σ	1.94σ	2.06σ	2.22σ
Parameter-space χ^2 (2 d.o.f.)	12.29	12.25	11.07	10.51
Parameter-space tension	$\mathbf{3.07\sigma}$	$\mathbf{3.06\sigma}$	$\mathbf{2.88\sigma}$	$\mathbf{2.79\sigma}$

Our estimated MDPS tension of 3.07σ for ΛCDM is higher than the 2.65σ reported by [53]. This is partly due to the removal of low-redshift data required by the z_0 approximation to the local void model. However, when assessing ΛCDM, we can include low-redshift CC measurements. We excluded them simply to ensure that the same data is used when comparing different z_0 scenarios. For better assessment of the BAO anomaly faced by ΛCDM, we extend the non-BAO dataset to include all 33 considered CC measurements [81,83]. In this case, the data-space tension becomes 1.94σ, while the parameter-space tension becomes 3.05σ. Both tensions are very slightly lower than for our extended redshift range. The MDPS tension of 3.05σ is higher than the previously reported 2.65σ [53]. This could be due to a much more modern calculation of the recombination temperature (Appendix A) and a more accurate treatment of neutrinos (Appendix B).

3.4. Bayesian Evidence

Since our analysis infers a very slightly negative z_0 while a local void requires a positive value, the data considered here do not, by themselves, prefer the addition of z_0 as an extra model parameter. To quantify this, we compute the Bayesian evidence of each model (Equation (21)). The results in Table 5 show that adding z_0 as a free parameter reduces Z by around 2 natural units (nats). If z_0 is fixed to 0.5%, there is a loss of only 0.37 nats, which rises to 0.82 nats when fixing z_0 to the previously expected 0.84%. These very small differences in Z indicate that the considered data are presently not discriminating enough to tell whether $z_0 = 0.84\%$, but this remains allowed.

Table 5. The natural logarithmic Bayesian evidence for different datasets and assumed z_0 scenarios (Equation (21)). Results are shown relative to the corresponding ΛCDM model, whose uncertainty of 0.16 is not included here.

Assumed z_0 Value	**Dataset Considered for Analysis**	
	$z > 0.5$ (Nominal)	**$z > 0.29$**
0 (ΛCDM)	–	–
Free	-1.99 ± 0.17	-2.32 ± 0.17
0.005	-0.37 ± 0.16	-0.20 ± 0.16
0.0084	-0.82 ± 0.16	-0.96 ± 0.16

In both our analysis and that of [53], local cz' measurements are not included because ΛCDM cannot fit these simultaneously with the other datasets, making it unphysical to calibrate the ΛCDM parameters using, e.g., both the CMB and the local cz'. However, this approach should be followed in models that can solve the Hubble tension, since data should obviously generally be included if at all possible. The local cz' constraint is indirectly included in our results through the choice of $z_0 = 0.84\%$ [73]. In the future, we hope to directly address local cz' constraints using a more advanced void model with outflows, which must be included to address the distance ladder.

3.5. Results Including DES-Dovekie SNe

We extend our main analysis by including likely SNe Ia from the DES-Dovekie catalogue [96,97]. Even with our extended redshift range, the redshift floor of 0.29 is high enough to exclude all external or legacy SNe in the catalogue, helping to ensure its homogeneity by involving only the DES photometric filter system. Since the SNe are not always spectroscopically confirmed, we restrict our attention to only those SNe with a $\geq 90\%$ probability of being Type Ia.

The predicted luminosity distance (D_L) is found as follows:

$$D_L(z_{\rm HD}, z_{\rm hel}) \;=\; (1 + z_{\rm hel}) D_c(z_{\rm c}), \tag{23}$$

where the heliocentric redshift ($z_{\rm hel}$) is corrected for small-scale peculiar velocities to obtain $z_{\rm HD}$, which is then used to estimate the cosmic redshift ($z_{\rm c}$) by applying Equation (3). As with other datasets, we only consider SNe with sufficiently large $z_{\rm HD}$ values for the z_0 approximation to be accurate. We use the predicted D_L to obtain a predicted distance modulus, which we compare to the observed value using the published precision or inverse covariance matrix. Since the DES catalogue lacks any absolute calibration, we add a magnitude offset with a wide uniform prior to the published distance moduli, which assume a particular arbitrary calibration. Since this offset is arbitrary, we marginalise over it. We note that although the SNe Ia are uncalibrated, combining with other datasets assuming the validity of ΛCDM at early times effectively does impose a calibration via the inverse distance ladder.

Figure 4 shows the triangle plot from our nested sampling run with free z_0. The parameters are summarised in Table 6. Including DES-Dovekie SNe Ia leads to tighter constraints, especially with our extended redshift range. However, the central parameter values do not change much, with the z_0 posterior still peaking close to 0. This leads to just over 2σ tension with the previously predicted value of 0.84% [73]. The posterior likelihood of an even higher z_0 is 1.20%, indicating that $z_0 = 0.84\%$ cannot be excluded at the 99% confidence level, even if we use our extended redshift range and include DES-Dovekie SNe Ia. If we do not include SNe, the likelihood that $z_0 > 0.84\%$ rises to $P(z_0 > 0.0084) = 9.00\%$ for our extended redshift range, indicating that SNe disfavour the previously predicted z_0. Interestingly, this is not the case for our nominal redshift range, where including DES-Dovekie SNe Ia raises $P(z_0 > 0.84\%)$ from 7.27% to 9.74%. This is because although SNe do tighten the error bars, they also increase the inferred value of z_0 for the nominal redshift range, while the opposite occurs for the extended redshift range. Given that the z_0 approximation might be inaccurate for the extended redshift range (Section 2.1), a more detailed analysis is required to assess whether SNe favour the local void scenario.

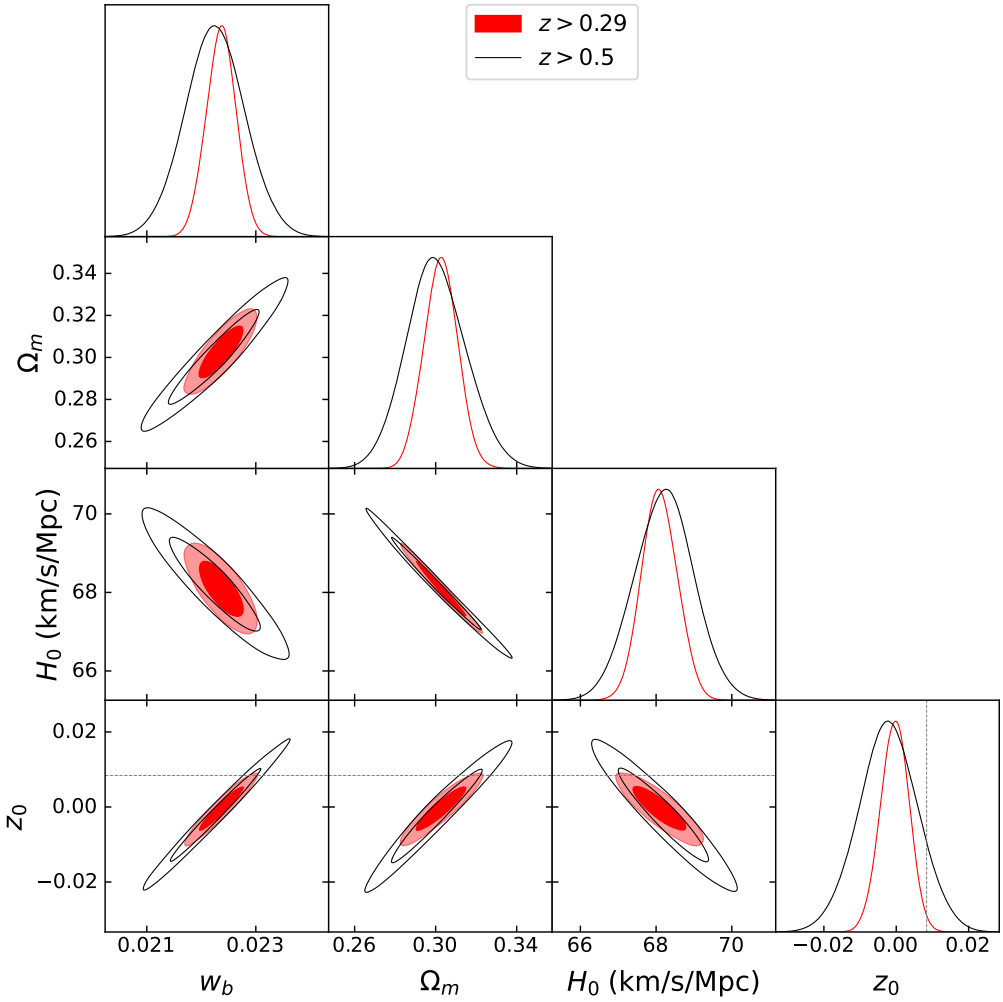


Figure 4. Triangle plot shown similarly to Figure 2 including also DES-Dovekie SNe Ia. The posteriors are now tighter than before, but the previously predicted $z_0 = 0.84\%$ is still allowed at just over 2σ.

Table 6. Inferred parameter values under different assumed z_0 scenarios for the nominal redshift range (top) and extended redshift range (bottom), including DES-Dovekie SNe Ia in the analysis. This leads to tighter constraints (c.f., Table 2).

		Assumed Value of z_0		
Parameter	**Free z_0**	**0 (ΛCDM)**	**0.005**	**0.0084**
		$z > 0.5$ dataset		
w_b	0.02225 ± 0.00054	0.02239 ± 0.00009	0.02272 ± 0.00008	0.02295 ± 0.00009
Ω_m	$0.300^{+0.015}_{-0.014}$	0.304 ± 0.004	0.313 ± 0.004	0.319 ± 0.004
H_0 (km/s/Mpc)	$68.21^{+0.76}_{-0.80}$	$68.02^{+0.26}_{-0.27}$	67.57 ± 0.25	67.28 ± 0.25
z_0	-0.0022 ± 0.0081	–	–	–
		$z > 0.29$ dataset		
w_b	0.02236 ± 0.00027	0.02239 ± 0.00009	0.02272 ± 0.00008	0.02294 ± 0.00009
Ω_m	0.303 ± 0.008	0.303 ± 0.003	0.313 ± 0.003	0.320 ± 0.003
H_0 (km/s/Mpc)	$68.09^{+0.48}_{-0.47}$	68.05 ± 0.24	$67.53^{+0.24}_{-0.24}$	$67.18^{+0.24}_{-0.23}$
z_0	-0.0004 ± 0.0039	–	–	–

3.6. Results Excluding the LRG2 BAO Measurement

The low measured D_V/r_d at $z = 0.7$ slightly reduces the inferred z_0 (Figure 3). This may explain why the best-fit $z_0 < 0$ with our nominal redshift range. The inferred z_0 is not as negative with our extended redshift range, presumably due to the slightly low D_V/r_d measurement at $z = 0.295$ pushing up z_0. We note that other D_V/r_d measurements at $z \approx 0.7$ are all higher than reported by DESI DR2, typically by around 2–3% (Figure 1).

If the DESI DR2 measurement of D_V/r_d at $z = 0.7$ is, indeed, revised upwards in the future and ends up more in line with pre-DESI results, this would reduce the tension for both ΛCDM and the $z_0 = 0.84\%$ model. It would also increase the inferred z_0, which might then be in better agreement with the predicted 0.84%.

Given the somewhat anomalous nature of the luminous red galaxy (LRG) 2 BAO measurement from DESI DR2 at $z = 0.7$, we redo our free z_0 analysis without the BAO angular scale and redshift depth measurements at this redshift. The z_0 inference is summarised in Table 7 for our nominal and extended redshift without and with DES-Dovekie SNe Ia. Although the results are consistent with $z_0 = 0$ in all cases, the inferred z_0 is slightly higher as a result of excluding the LRG2 BAO measurement (c.f., Table 2)—as one might expect from Figure 3. The preference for a higher z_0 is especially apparent if we neglect SNe and use our extended redshift range. However, once SNe are included, the z_0 posterior peak remains close to 0, even if we exclude LRG2. Removing this point has only a modest impact on the results with SNe. Even so, it will still be important to revisit our analysis once updated BAO measurements become available.

Table 7. The inferred value of z_0 in analysis variants excluding the LRG2 BAO measurement from DESI DR2 at $z = 0.7$, motivated by previous measurements at a similar redshift being systematically higher (Figure 1). Different rows show results without and with DES-Dovekie SNe Ia (Section 3.5). Compared to results including the LRG2 BAO measurement (Tables 2 and 6), the inferred z_0 is slightly higher, especially for our extended redshift range without SNe. However, z_0 remains consistent with 0 in all cases, especially once SNe are included.

	Dataset Considered for Analysis	
	$z > 0.5$ **(Nominal)**	$z > 0.29$
Without SNe	-0.003 ± 0.011	0.004 ± 0.007
With SNe	$-0.0004^{+0.0095}_{-0.0093}$	$0.0010^{+0.0038}_{-0.0040}$

4. Discussion

4.1. Implications for the Local Void Scenario

Our results demonstrate that the latest $z > 0.5$ measurements provide a sub-percent constraint on any fixed non-cosmological contribution to the redshift of distant sources. In the local void scenario, it was expected that this contribution would be $z_0 = 0.84\%$ (Section 5.3.3 of [73]). This remains plausible for both our nominal and extended redshift ranges (bottom-right panel of Figure 2). Interestingly, the most likely z_0 inferred by our analysis increases slightly in the latter case, lining up better with the predicted 0.84%. This shows that the spillover effects of a local void at high redshift remain consistent with the latest observations. However, our results prefer the ΛCDM value of $z_0 = 0$, causing the Bayesian evidence to disfavour the addition of z_0 as an extra model parameter (Table 5).

Our reconstructed $\alpha_{\rm iso}(z)$ shows that ΛCDM can adequately match the available BAO observations, as shown by the horizontal line at unity passing through most of the DESI DR2 measurements in Figure 3. The fiducial cosmology used to normalise the predicted D_V/r_d differs slightly from the parameters that best fit the CMB, but the total χ^2 is still quite acceptable (Table 3). Fixing z_0 to 0.5% or 0.84% slightly increases the total χ^2, but this remains well within acceptable bounds. Interestingly, the higher χ^2 arises despite a better fit to the CMB. This is because of a worse fit to DESI DR2, as shown in Figure 3.

The mild tension faced by both ΛCDM and the considered z_0 models is clearly largely driven by the anomalously low D_V/r_d measurement at $z = 0.7$, though the low measurement at $z = 0.9$ also contributes somewhat. While there are few pre-DESI measurements at $z = 0.9$ with which to compare, there are several measurements at $z = 0.7$ (Figure 1). These measurements are generally about 2–3% higher than reported by DESI DR2. A recent

reanalysis of DESI DR1 using a covariance matrix estimated from mock catalogues also gives a result about 2% higher than if DESI DR2 results are linearly interpolated to the same redshift [107]. This makes it likely that the DESI DR2 measurement at $z = 0.7$ will be revised upwards by about this amount in future data releases, reducing the mild tension faced by both ΛCDM and the void models. We note that the inferred z_0 is clearly dragged down by the low DESI measurement at $z = 0.7$, since reducing z_0 to negative values provides a better fit to this point (Figure 3). We therefore expect the posterior inference on z_0 to shift upwards in the future, which might then line up even better with the prediction of the local void scenario. We explore this possibility by inferring z_0 without the LRG2 BAO measurement (Section 3.6). This does, indeed, increase the inferred z_0, but including DES-Dovekie SNe Ia reduces it to almost exactly 0.

Our results in Figure 3 show little visible sign of the controversial BAO anomaly, a claimed internal inconsistency between high-redshift datasets in ΛCDM. However, this has to be assessed following the usual scientific method of making predictions in advance of the observations used to test a model – or at least by setting up the model without using those observations. This procedure was discussed in detail in Section 5 of [53]. The corresponding results in the z_0 model are presented in Section 3.3. With our nominal redshift range, ΛCDM faces an MDPS tension of 3.01σ, which rises to 3.07σ with our extended redshift range. Focusing on the latter because it includes all 13 DESI DR2 BAO measurements, we find that the local void model can reduce this tension down to 2.79σ if $z_0 = 0.84\%$. This is despite a slight increase in data-space tension from 1.95σ to 2.22σ, but this is not the MDPS tension (Table 4). Our results imply that although the local void model slightly worsens the fit to the data in terms of χ^2 and ability to predict the DESI observations, it reduces the gap between BAO and non-BAO datasets in the standard $(H_0 r_\mathrm{d}, \Omega_\mathrm{m})$ parameter space commonly used for BAO problems. The reduced parameter-space tension cannot be explained by inflated uncertainties because these are almost the same regardless of whether we fix $z_0 = 0$ or 0.84% (Table 2). The latter gives a lower MDPS tension, but BAO and non-BAO datasets are inconsistent at the 99% confidence level in both scenarios. However, if we double the probability of consistency to account for the look-elsewhere effect associated with considering the maximum of two tension metrics, then the reduction in parameter-space tension that arises from fixing $z_0 = 0.84\%$ instead of 0 is sufficient to reconcile BAO and non-BAO datasets from $z > 0.29$ at the 99% confidence level. In short, despite the slightly worse fit to the data if $z_0 = 0.84\%$, the residuals with respect to observations look less systematic in standard ways of viewing BAO problems.

The local void model with $z_0 = 0.84\%$ performs quite well compared to the background solutions considered by [53]. Their Table 5 shows that each model with best-fitting values of its parameters usually predicts a BAO contribution to χ^2 exceeding 20, often by a substantial margin. This is not ideal for 13 d.o.f. The only exceptions are the Phen models, which assume a simple algebraic addition to the ΛCDM $H(z)$ (see their Equation (31)). The Phen, exp model achieves a BAO χ^2 of 19.24, while the Phen, sech model achieves 18.31. Our Table 3 shows that the best-fitting model with $z_0 = 0.84\%$ achieves a similar BAO χ^2 contribution of 18.61. This could be reduced further if the void parameters are optimised including BAO datasets, since it is quite possible that a different model with a reduced z_0 might still adequately fit the local cz' and galaxy number counts. For instance, if $z_0 = 0.5\%$, the BAO contribution to χ^2 drops to 16.79. Even without this, it is clear that the void model provides an adequate fit for 13 d.o.f.

To perform a comparison in terms of the MDPS BAO tension, we need to mimic our procedure of fixing z_0 to the best-fitting value based on non-BAO datasets. For this, we rerun the BAO tension calculation in [53] for two of the Phen models, fixing their two non-standard parameters to best-fitting values on the basis of all the non-BAO datasets

they considered. The third Phen model in their study is not shown here because it cannot solve the Hubble tension (the CMB contribution to χ^2 is 26.7 from 3 d.o.f.). The results for the other two models are shown in Table 8. As with ΛCDM, the MDPS tension comes from parameter space and is just under 2σ for both Phen models. According to this measure, the local void model with our extended redshift range and $z_0 = 0.84\%$ performs slightly worse, since it faces an MDPS tension of 2.79σ, also from parameter space (bottom part of Table 4). Moreover, the data-space tension is slightly higher in the void model compared to the Phen models from [53]. These small differences make it difficult to tell which is better from an observational perspective.

Table 8. BAO tensions for the Phen models considered by [53] which can solve the Hubble tension. The MDPS tension is highlighted in bold in each column.

	Phen Model [53]	
BAO Tension Metric	**Exp**	**Sech**
Data space χ^2 (13 d.o.f.)	18.98	21.55
Data-space tension	1.54σ	1.86σ
Parameter space χ^2 (2 d.o.f.)	5.00	6.03
Parameter-space tension	$\mathbf{1.74\sigma}$	$\mathbf{1.97\sigma}$

We suggest that the Phen models in [53] empirically capture how a local void distorts the distance–redshift relation. While their models can, of course, be interpreted as background solutions, this raises fine-tuning issues because the non-standard addition to $H(z)$ must decay rather rapidly with redshift, as captured by their z_1 parameter. Those authors inferred that $z_1 < 0.20$ at high confidence (see their Table 3). This is far below the redshift where dark energy changes the sign of $\ddot{a}$, raising the question of why departures from ΛCDM should arise only at such recent epochs. If this is the case, it would imply rather unusual behaviour for the effective dark energy equation of state (see their Figure 4). As argued by those authors, the low inferred z_1 is more naturally interpreted as capturing the impact of a local void rather than a genuine adjustment to the background $a(t)$.

While our goal here is to address the consistency of the local void model at high redshift, it is clear that its main impact would be at lower redshift, where a more detailed model would be required [73]. This would be particularly important if the DESI BAO measurements can be extended to lower redshift, where a larger deviation from ΛCDM is expected. Indeed, a generic consequence of a low-redshift solution to the Hubble tension is that $\alpha_{\rm iso} \approx 0.92$ at low redshift because inflating cz' by 9% would correspondingly reduce the distance to any given z [52]. Other tests of a local void are also possible at low redshift [76]. For instance, it is possible to reconstruct $\dot{a}(z)$ assuming ΛCDM at high redshift by allowing a flexible evolution for the dark energy equation of state [108–110]. These results can be cast in terms of how much deviation there is from the CMB-calibrated ΛCDM expectation using the concept of $H_0(z)$, the value of H_0 that would be inferred from extrapolation of data in a narrow redshift range centred on z down to $z = 0$, assuming ΛCDM [111,112]. The predicted $H_0(z)$ curve in the void model [7] is in good agreement with the observational reconstruction [109]. More recent results indicate even better agreement [110,113]. Importantly, the tendency for the reconstructed $H_0(z)$ to reach the community consensus on the local cz' as $z \to 0$ occurs without applying local cz' constraints [110]. Those authors only used uncalibrated SNe Ia combined with BAO assuming a standard $r_{\rm d}$, which effectively calibrates SNe Ia via the inverse distance ladder. Similar results can be obtained by taking the opposite approach, using the local cz' without assuming ΛCDM at high redshift [114]. These results make it likely that the solution to the Hubble tension lies at

low redshift, though the authors did not directly address whether this is through a local void or a late-Universe background solution.

One unusual aspect of the CMB that cannot easily be understood through modified $a(t)$ is the preference for a much lower H_0 and hotter CMB when the FIRAS prior is dropped [77]. Their Figure 3 shows that if we fix $(\widetilde{w}_\mathrm{b}, \widetilde{w}_\mathrm{bc}, \theta_\star)$, we can alter T_CMB without impacting the primary CMB anisotropies, but there is a small secondary effect on the power spectrum around a multipole moment of $\ell \approx 10$. This is due to the integrated Sachs–Wolfe (ISW) effect [115], which depends on the balance between matter and dark energy densities at late times. Since this is the only discernible impact on the CMB power spectrum if we move along the usual degeneracy between H_0 and T_CMB corresponding to fixed $(\widetilde{w}_\mathrm{b}, \widetilde{w}_\mathrm{bc}, \theta_\star)$, it seems likely that the inference of a hotter CMB is related to some difficulty faced by ΛCDM with the growth of structure on large scales. We note that the CMB temperature anomaly would be even larger than reported by Ivanov et al. [77] if they had allowed $\Omega_\mathrm{m} > 1$, since the posteriors on H_0 and T_CMB were clearly truncated by this prior, which lacks theoretical motivation (the cosmological constant could be negative). The large deviation from conventional estimates of H_0 and Ω_m is not a sign that these parameters could really be drastically different from ΛCDM but, instead, indicates that it faces a problem with the CMB power spectrum in the temperature-sensitive part at $\ell \approx 10$. This may be related to the enhanced growth of structure on large scales required for a local void to solve the Hubble tension. Since the details of the CMB power spectrum at these low multipoles depend on as yet unknown details of structure formation on large scales, our main analyses neglect the fact that altering T_CMB at fixed $(\widetilde{w}_\mathrm{b}, \widetilde{w}_\mathrm{bc}, \theta_\star)$ slightly alters the predicted CMB power spectrum at low ℓ values. The information content here is, in any case, far lower than in the primary CMB anisotropies, which are unaffected at fixed $(\widetilde{w}_\mathrm{b}, \widetilde{w}_\mathrm{bc}, \theta_\star)$ [77].

To obtain a more detailed prediction for the CMB power spectrum at low ℓ values, we would require a deeper theory where KBC-like voids are common, yet the background expansion history and early-Universe physics remain largely unchanged. Models that increase the frequency of extreme voids would inevitably also increase the frequency of extreme overdensities, perhaps explaining the properties of the El Gordo massive galaxy cluster collision better than ΛCDM, which struggles to explain its high redshift, mass, and collision velocity [116,117]. It has even been proposed that relaxing the assumption of independence between modes on different wavelengths could jointly solve the Hubble tension and the cosmic radio dipole anomaly, an unexpectedly large dipole amplitude in radio-source number counts at cosmological distances [118–122]. Both tensions could be assigned to $\lesssim 2\sigma$ cosmic variance if it is enhanced in this way [123].

4.2. Implications for Theories Other than a Local Void

The limits that we place on z_0 limit the scope for theories that enhance the growth of structure too much, as that would make it unlikely for z_0 to be as small as our results imply (c.f. [124]). Indeed, the main reason the Haslbauer et al. [73] model predicts z_0 at an almost observable level is their use of MOND-inspired equations to enhance the gravitational field of a given (under)density distribution on scales $\gtrsim$100 Mpc. Thus, the Haslbauer et al. [73] model has both a larger and deeper underdensity than allowed in ΛCDM, as well as stronger outward gravity, even for the same underdensity.

To illustrate this, we can consider the predicted z_0 if there is a standard relation between the gravitational field and the density distribution sourcing it. Though we assume that density variations exist only in the matter component, our derivation works similarly

if the underdensity is, instead, in the dark energy distribution [125]. The gravitational field (g) at a distance of r from a spherically symmetric fractional underdensity (δ) is

$$g = \frac{4\pi G r \bar{\rho} \delta}{3}, \tag{24}$$

where $\bar{\rho}$ is the cosmic average matter density. Assuming the void has a size of r_v and integrating Equation (24) once to obtain the central potential (Φ_0), we can estimate that

$$z_0 = \frac{\Phi_0}{c^2} = \frac{1}{4}\left(\frac{r_v}{r_H}\right)^2 \Omega_\mathrm{m}\, \delta, \tag{25}$$

where $r_H \equiv c/H_0$, using the fact that $\bar{\rho} \equiv 3H_0^2\Omega_\mathrm{m}/(8\pi G)$. Assuming that $H_0 = 70$ km/s/Mpc and $\Omega_\mathrm{m} = 0.3$, our constraint that $|z_0| \lesssim 0.01$ (Table 2) implies that

$$|\delta| \lesssim 2.5\left(\frac{1\,\mathrm{Gpc}}{r_v}\right)^2. \tag{26}$$

This constraint is very weak for any structure that can be described as local or non-cosmological, indicating that our limit on $|z_0|$ is not particularly helpful in standard gravity. This is the case even if we assume the density variation actually lies in the dark energy, since that would just replace $\Omega_\mathrm{m} \to \Omega_\Lambda$, leaving our result qualitatively unchanged.

Our constraints on z_0 are far more relevant to modified theories of gravity in which it is stronger than in standard theory on very large scales. The ultimate detection of z_0 at the $\mathcal{O}(10^{-3})$ level would suggest that the effective G relevant to the growth of structure on scales $\gtrsim 100$ Mpc is different from the G entering the Friedmann equation. In the context of the local void model, our z_0 constraint places a limit on the void size because $z_0 \underset{\sim}{\propto} r_v^2$ (Equation (25)). Incorporating the techniques developed here into the Haslbauer et al. [73] analysis would naturally rectify its tendency to drift towards very large r_v values (see their Appendix C).

We have assumed that any local structure would be contained within $z \lesssim 0.3$, enabling us to use the z_0 approximation (Equation (3)). This would not be true in scenarios where there is a very long wavelength perturbation imprinted by inflationary physics. In this case, we could make the opposite approximation that any local potential hill would extend out much farther than the most distant BAO data point at $z = 2.3$. In this case, the z_0 term would still affect the CMB and the r_d calculation, but it should not be considered when calculating CC and BAO predictions. This is because there would be little potential difference between us and any sources at $z < 2.3$. Our analysis would need to be redone with this revised structure to test such models, though it is possible that stronger constraints can be obtained from the kinematic Sunyaev–Zel'dovich (kSZ) effect [126]. kSZ constraints still allow a void similar to the KBC void, but a much larger and deeper void is excluded [127,128]. A similar argument would apply to a local overdensity, which would create a kSZ signal of the opposite sign. Constraints from the kSZ effect probe peculiar velocities generated by a potential gradient, while z_0 constraints directly probe potential differences through impacts like a hotter predicted CMB and reduced r_d, issues we have considered in some detail.

Although our focus has been on GR, there is also a kinematic contribution to the redshift. This is generally expected to be small at the distances considered here, even in the local void scenario [52]. However, it has been proposed that the cosmic radio dipole anomaly is caused by substantial velocity between the quasar rest frame and the CMB, which would create angular variation in number counts due to special relativistic beaming effects [129,130]. This kinematic interpretation is by no means necessary, even if the cosmic radio dipole anomaly is confirmed, since the dipole in number counts could be

intrinsic [123,131]. In the kinematic interpretation, there would be an interesting interplay with BAO observations because these generally cover only a small portion of the sky. A coherent bulk flow on such large scales could then create an extra contribution to the redshift, distorting the relation between redshift and the BAO observables. However, even a bulk flow of 1000 km/s is still only $0.003\,c$, so the effect ought to be well below our uncertainty on z_0. This is especially true given that much of the impact of z_0 on our analysis stems from the hotter predicted CMB, which would not arise in this scenario, given CMB observations cover the whole sky. It is also unclear how a coherent bulk flow could arise on the very large scales relevant to DESI DR2 BAO observations, though this should be tested by checking for anisotropy in the BAO angular scale and redshift depth once deep BAO surveys cover more of the sky.

5. Conclusions

There is now a considerable body of evidence that the local $cz' > H_0^{\rm CMB}$ (Section 1). This Hubble tension might arise due to outflow from a local void (as reviewed in [76]). As with all models to inflate the local cz', there are inevitably spillover effects at high redshift. We test the consistency of the local void model using the wealth of high-z data that has recently become available, including BBN, CMB, CC, and especially BAO measurements from DESI DR2 [50]. It was previously claimed that the local void model from [73] provides a better fit than ΛCDM to BAO measurements over the last 20 years [52]. We assess this claim in more detail by including several effects that those authors did not account for.

To simplify our analysis, we approximate a local void only affecting the redshift through a fixed additional GR contribution of z_0, keeping only the GR term in Equation (2). Figure 1 shows that this is a good approximation at $z > 0.5$, where a local void would have little physical effect. Its main impact on observations of such distant sources would be through the GR contribution arising from photons being repelled by the outward gravity of a local void. We therefore approximate a local void using the z_0 model (Equation (3)). We argue in Section 2.1 that this may still be reasonably accurate down to $z = 0.29$, permitting comparison with all 13 DESI DR2 BAO measurements and benefiting from several additional CC measurements (Section 3).

Our main result is that $z_0 = -0.004^{+0.008}_{-0.009}$ with data from our nominal redshift range, rising to $z_0 = -0.001 \pm 0.007$ for our extended redshift range. In both cases, the results are in good agreement with the prior expectation that $z_0 = 0.0084$ based on fitting of the local cz' and galaxy number counts without considering BAO datasets (Section 5.3.3 of [73]). A slightly better fit can be obtained in a different void model with $z_0 = 0.005$ if it still matches the local constraints. This might arise due to a smaller void (as suggested by [78]). In either case, the best-fitting models are in good agreement with DESI DR2 (Figure 3) and provide an acceptable χ^2 (Table 3).

It has been claimed that ΛCDM suffers from an internal tension between BAO and other high-redshift datasets. This BAO anomaly arises when considering the ability of ΛCDM to predict BAO data on the basis of non-BAO datasets [53]. Applying their approach to data from our extended redshift range so that all DESI DR2 measurements can be addressed, we find that ΛCDM faces an MDPS tension of 3.07σ from the standard $(H_0 r_{\rm d}, \Omega_{\rm m})$ parameter space. In the local void model with $z_0 = 0.84\%$, this decreases to 2.79σ, which now lies within the 99% credible region if the tail probability is doubled to account for the look-elsewhere effect associated with considering the maximum of two tension metrics. This is not the case for ΛCDM. The BAO anomaly is not apparent in data space, where ΛCDM faces a tension of only 1.95σ for our extended redshift range. Interestingly, the void model actually increases this to 2.22σ, indicating that it navigates the

subtle tradeoffs between data- and parameter-space tensions to reduce the MDPS tension, which is conventionally used to quantify the BAO anomaly.

Fixing z_0 to the 0.84% level predicted by a model previously shown to fit local constraints quite well (Section 5.3.3 of [73]), we find an MDPS BAO tension of only 2.79σ and acceptable χ^2 contributions from BBN, CMB, BAO, and CC in the best-fitting model (Table 3). Despite the non-standard prediction of a slightly hotter CMB and reduced r_d, fixing $z_0 = 0.84\%$ does not cause conflict with the high-redshift datasets considered here. It is also possible that a different void model could acceptably fit local constraints with a reduced z_0 of perhaps 0.5%, which would fit the data better but mildly increase the MDPS tension to 2.88σ. We therefore conclude that the local void model remains consistent with high-redshift datasets despite their high precision and, at best, modest deviations from the best-fit ΛCDM model.

These results motivate a more thorough analysis of the void scenario beyond the high-redshift approximation adopted here, since its primary impact occurs at low redshift, where a more detailed model including outflows is required to assess its viability in light of the Hubble tension. A valuable dataset in this context is the CF4 galaxy catalogue of redshifts and redshift-independent distances [132]. This was used to show that any local void in a background *Planck* cosmology should be smaller and perhaps deeper than claimed by [73], but the local cz' over the 100–600 Mpc range typically used to measure it can still be as high as 73 km/s/Mpc within the 1σ error bar for one of the three considered void density profiles [78]. We are also exploring if the rapid return to the *Planck* cosmology predicted by the local void scenario is consistent with DESI CC measurements at $z < 0.2$ [83].

Author Contributions: Conceptualization, I.B. and J.A.N.; methodology, I.B. and J.A.N.; software, I.B. and J.A.N.; validation, I.B. and J.A.N.; formal analysis, J.A.N.; investigation, J.A.N.; resources, H.D.; writing—original draft preparation, I.B.; writing—review and editing, I.B., J.A.N. and H.D.; visualization, J.A.N.; supervision, I.B. and H.D.; project administration, H.D.; funding acquisition, H.D. All authors have read and agreed to the published version of the manuscript.

Funding: All authors are supported by Royal Society University Research Fellowship grant 211046.

Data Availability Statement: Our code is publicly available https://github.com/antonionajeraq/z0_local_void_BAO.git, accessed on 26 July 2026. This includes the main cosmological analysis and scripts to extract CLASS recombination and decoupling temperatures over a parameter grid, fit the results using a quadratic form, then print out the rms and maximum absolute residual. The datasets used in this work are publicly available and come from the cited publications.

Acknowledgments: The authors are grateful to the anonymous referees for comments which helped to substantially improve this manuscript.

Conflicts of Interest: The authors declare no conflicts of interest.

Appendix A. The Recombination and Decoupling Temperatures in ΛCDM

Most solutions to the Hubble tension are at the background level, in which case $z_0 = 0$ and $T_\mathrm{CMB} = T_\mathrm{FIRAS}$. For the benefit of readers, here, we provide fitting formulae for the recombination and decoupling temperatures as a function of $(w_\mathrm{b}, w_\mathrm{bc})$, with our grid still centred on (0.0225, 0.1450) as before. Though z_0 is no longer a parameter, $T_\star$ should still be found using Equation (17), with T_d found analogously.

The reference recombination temperature is now $T_\star^\mathrm{ref} = 2970.29$ K, while its gradient and Hessian become

$$\boldsymbol{g}_\star = \begin{pmatrix} -3188.92 \\ 194.09 \end{pmatrix}, \quad \mathbf{H}_\star = \begin{bmatrix} 265960.27 & -7860.93 \\ -7860.93 & -488.36 \end{bmatrix}. \tag{A1}$$

The reference decoupling temperature is now $T_{\rm d}^{\rm ref} = 2892.74$ K, while its gradient and Hessian become

$$\boldsymbol{g}_{\rm d} = \begin{pmatrix} 5925.64 \\ 203.34 \end{pmatrix}, \quad \mathbf{H}_{\rm d} = \begin{bmatrix} -189076.80 & -4767.87 \\ -4767.87 & -626.49 \end{bmatrix}. \tag{A2}$$

These results are very similar to those used in our main analysis if we simply set $z_0 = 0$, but fixing this when calculating our CLASS grid improves the accuracy slightly in studies that assume homogeneity. This is evident in that the maximum (rms) error in $T_\star$ across our grid is now only 0.68 (0.23) mK, while the maximum (rms) error in $T_{\rm d}$ is only 0.80 (0.32) mK.

Appendix B. Evolution of the Neutrino Density

We assume a standard background cosmology similarly to [53], but we make a small refinement to the handling of neutrinos in their Appendix B. Since the neutrino energy density is defined relative to that in photons, we briefly recap the photon energy density. Expressed as an equivalent mass density, this is

$$\rho_\gamma = \frac{\pi^2 k^4}{15\hbar^3 c^5} T_{\rm CMB}^4 , \tag{A3}$$

where k is Boltzmann's constant, $\hbar$ the reduced Planck constant, and $T_{\rm CMB}$ the temperature of the CMB (Equation (11)). The photon number density (n_γ) follows from standard blackbody physics.

$$n_\gamma = \frac{2\zeta(3)}{\pi^2} \left(\frac{kT_{\rm CMB}}{\hbar c} \right)^3 , \tag{A4}$$

where $\zeta(3) = 1.202$ is the Riemann zeta function with argument 3.

Neutrinos behave like photons at high redshift. The ultra-relativistic neutrino density in species i is

$$\rho_{\nu,{\rm ur},i} \equiv \rho_\gamma R_{\nu_i/\gamma} . \tag{A5}$$

We designate the neutrino species as A, B, and C in descending order of rest mass. The ur subscript indicates that the ratio of $R_{\nu_i/\gamma}$ between the photon density and that in neutrino species i is applicable only in the early Universe, when neutrinos were ultra-relativistic. Using quantum statistics, we obtain

$$R_{\nu_i/\gamma} = \frac{7}{8} \left(\frac{4}{11} \right)^{4/3} \frac{N_{\rm eff}}{3} , \tag{A6}$$

where $N_{\rm eff} = 3.044$ is effectively the number of neutrino species around the time of recombination [133–135].

In the non-relativistic regime, the neutrino density in species i is given by

$$\rho_{\nu,i} = n_{\nu,i} m_{\nu,i} , \tag{A7}$$

where $m_{\nu,i}$ is the neutrino mass of flavour i and $n_{\nu,i}$ is the number density of such neutrinos, which is given by

$$n_{\nu,i} = \frac{3}{11} n_\gamma \left(\frac{N_{\rm eff}}{3} \right)^{0.68} . \tag{A8}$$

If the neutrinos were thermalised, the exponent here would be 3/4. We use a smaller exponent of 0.68 to ensure that, in the non-relativistic limit, $w_\nu = \sum_i m_{\nu,i}c^2/(93.14\,\mathrm{eV})$ [136]. The lower exponent arises because the energy from electron–positron annihilation mostly goes into the high-energy tail of the neutrino energy distribution, which does not have enough time to thermalise before neutrino decoupling.

Unlike photons, which are always relativistic, massive neutrinos of species i become non-relativistic when the cosmic scale factor is

$$a_{nr,i} = \frac{1}{\sqrt{\left(\left.\frac{\rho_{\nu,i}}{\rho_{\nu,\mathrm{ur},i}}\right|_{a=1}\right)^2 - 1}}. \tag{A9}$$

We use the following form for the transition between relativistic and non-relativistic behaviour:

$$\rho_{\nu,i} = \frac{\rho_{\nu,\mathrm{ur},i}|_{a=1}}{a^4}\sqrt{1+\left(\frac{a}{a_{\mathrm{nr},i}}\right)^2}. \tag{A10}$$

This only applies to massive neutrinos, which consequently have a present neutrino density of $\rho_{\nu,i} \gg \rho_{\nu,\mathrm{ur},i}$, what the neutrino density would have been if the neutrinos were massless. For any massless species, the behaviour is identical to radiation:

$$\rho_{\nu,i} = \frac{\rho_{\nu,\mathrm{ur},i}|_{a=1}}{a^4}. \tag{A11}$$

Nájera et al. [53] assumed, for simplicity, that all the neutrino species have the same mass, so $m_{\nu,i} = (20, 20, 20)\ \mathrm{meV}/c^2$. We replace this with the much more realistic assumption that $m_{\nu,i} = (50, 10, 0)\ \mathrm{meV}/c^2$, as indicated by terrestrial neutrino experiments if neutrino rest masses are kept as low as possible, implying we need to use the normal hierarchy or mass ordering. The neutrino mass sum therefore remains $\sum m_\nu = 60\ \mathrm{meV}/c^2$, matching [53] and most other studies.

Equation (A10) can be generalised to

$$\rho_{\nu,i} = \frac{\rho_{\nu,\mathrm{ur},i}|_{a=1}}{a^4}\left[1+\left(\frac{a}{a_{\mathrm{nr},i}}\right)^{k_\nu}\right]^{1/k_\nu}. \tag{A12}$$

Following [53], we assume that the transition of neutrinos from relativistic to non-relativistic has a sharpness of $k_\nu = 2$. We can obtain a better fit to detailed calculations using Fermi–Dirac statistics if we use $k_\nu = 1.83$ (Equation (26) of [137]). However, we will see below that this makes very little difference to the results. We therefore assume that $k_\nu = 2$, which is much cheaper computationally because it avoids the use of fractional powers.

Appendix C. Accuracy of the Compressed CMB Likelihood

An important improvement over [53] is that the recombination temperature is found using a quadratic fit to CLASS results rather than based on an ancient fitting formula [8]. To better line up with modern results and include three decades of progress on the atomic physics constants and other factors relevant to recombination, Nájera et al. [53] adapted the formula slightly by changing a fixed factor of $1048 \to 1045$ in their Equation A10. In our approach, such a 'fix' is not necessary, but it is still important to check the accuracy of our approach in some way.

We infer H_0, w_b, and w_bc in ΛCDM using the compressed CMB likelihood (Equation (14)). Since the preferred values and covariance matrix are obtained from the

chains in [12] without using their reported H_0, we can compare this to our H_0 inference. The results are shown in Table A1 for different assumed values of k_ν and the neutrino masses, with $\sum m_\nu = 60$ meV$/c^2$ in all cases. The first column shows $m_{\nu,A}$, the mass of the most massive neutrino species. We assume this is the only massive neutrino, species A and B are the only massive neutrinos, or that all three species are equally massive (as assumed in [53]). Our nominal assumption is that $m_{\nu,A} = 50$ meV$/c^2$ and $m_{\nu,B} = 10$ meV$/c^2$, with species C being massless. Our results are barely affected by whether we choose $k_\nu = 1.83$ or 2, so we choose the latter to reduce complexity.

Table A1. The inferred value of H_0 with fixed $\sum m_\nu = 60$ meV$/c^2$ but different masses for the most massive neutrino, as indicated in the first column. In the 50 meV$/c^2$ case, another species has a mass of 10 meV$/c^2$, while the third species is massless. All neutrinos are equally massive in the 20 meV$/c^2$ case. The sharpness of the relativistic-to-non-relativistic transition is governed by the k_ν parameter (Equation (A12)).

Max. m_ν (meV/c^2)	**Transition Sharpness**	
	$k_\nu = 1.83$	$k_\nu = 2$
60	$67.20^{+0.37}_{-0.41}$	67.18 ± 0.39
50	$67.18^{+0.41}_{-0.36}$	$67.19^{+0.41}_{-0.36}$
20	67.24 ± 0.39	$67.27^{+0.38}_{-0.41}$

The SPT-3G Collaboration SPT-3G Collaboration [12] implicitly assumed that species B and C are massless, recovering $H_0 = 67.19 \pm 0.38$ km/s/Mpc in this case. Our compressed CMB likelihood approach is able to recover this value and uncertainty to an accuracy of 0.01 km/s/Mpc, which is a negligibly small difference. This demonstrates the reliability of our much simpler system of equations, which bypasses calls to CLASS in the likelihood function and does not involve comparison with the full CMB power spectrum. Although we assume that $m_{\nu,A} = 50$ meV$/c^2$ and $m_{\nu,B} = 10$ meV$/c^2$, the results are barely affected by instead assuming that only species A is massive while keeping $\sum m_\nu$ fixed. However, there is a noticeable difference if we assume that all three species are equally massive, despite fixing $\sum m_\nu$. This means that although details of the relativistic-to-non-relativistic neutrino transition are far less important for cosmology than $\sum m_\nu$, it is still important to assign the vast majority of $\sum m_\nu$ to just one species, as indicated by terrestrial neutrino experiments if we make the usual assumption that neutrino masses should be kept as low as possible. This assumption is called the normal mass ordering, which can be distinguished from the inverted mass ordering with a few years of data from the recently constructed Jiangmen Underground Neutrino Observatory (JUNO; [138]).

Notes

[1] https://dynesty.readthedocs.io/en/v2.1.5/, accessed on 26 July 2026.
[2] https://getdist.readthedocs.io/en/latest/, accessed on 26 July 2026.

References

1. Wirtz, C. Einiges zur Statistik der Radialbewegungen von Spiralnebeln und Kugelsternhaufen. *Astron. Nachrichten* **1922**, *215*, 349. [CrossRef]
2. Wirtz, C. De Sitters Kosmologie und die Radialbewegungen der Spiralnebel. *Astron. Nachrichten* **1924**, *222*, 21. [CrossRef]
3. Di Valentino, E.; Said, J.L.; Riess, A.; Pollo, A.; Poulin, V.; Gómez-Valent, A.; Weltman, A.; Palmese, A.; Huang, C.D.; van de Bruck, C.; et al. The CosmoVerse White Paper: Addressing observational tensions in cosmology with systematics and fundamental physics. *Phys. Dark Universe* **2025**, *49*, 101965. [CrossRef]

4. Casertano, S.; Anand, G.; Anderson, R.I.; Beaton, R.; Bhardwaj, A.; Blakeslee, J.P.; Boubel, P.; Breuval, L.; Brout, D.; H0DN Collaboration; et al. The Local Distance Network: A community consensus report on the measurement of the Hubble constant at ∼1% precision. *Astron. Astrophys.* **2026**, *708*, A166. [CrossRef]
5. Efstathiou, G.; Sutherland, W.J.; Maddox, S.J. The cosmological constant and cold dark matter. *Nature* **1990**, *348*, 705. [CrossRef]
6. Ostriker, J.P.; Steinhardt, P.J. The observational case for a low-density Universe with a non-zero cosmological constant. *Nature* **1995**, *377*, 600–602. [CrossRef]
7. Mazurenko, S.; Banik, I.; Kroupa, P. The redshift dependence of the inferred H_0 in a local void solution to the Hubble tension. *Mon. Not. R. Astron. Soc.* **2025**, *536*, 3232–3241. [CrossRef]
8. Hu, W.; Sugiyama, N. Small-Scale Cosmological Perturbations: An Analytic Approach. *Astrophys. J.* **1996**, *471*, 542. [CrossRef]
9. Eisenstein, D.J.; Hu, W. Baryonic Features in the Matter Transfer Function. *Astrophys. J.* **1998**, *496*, 605. [CrossRef] [PubMed]
10. Aghanim, N.; Akrami, Y.; Ashdown, M.; Aumont, J.; Baccigalupi, C.; Ballardini, M.; Banday, A.J.; Barreiro, R.B.; Bartolo, N.; Planck Collaboration VI; et al. Planck 2018 results. VI. Cosmological parameters. *Astron. Astrophys.* **2020**, *641*, A6. [CrossRef]
11. Louis, T.; La Posta, A.; Atkins, Z.; Jense, H.T.; Abril-Cabezas, I.; Addison, G.E.; Ade, P.A.R.; Aiola, S.; Alford, T.; Alonso, D.; The Atacama Cosmology Telescope Collaboration; et al. The Atacama Cosmology Telescope: DR6 power spectra, likelihoods and ΛCDM parameters. *J. Cosmol. Astropart. Phys.* **2025**, *2025*, 062. [CrossRef]
12. Camphuis, E.; Quan, W.; Balkenhol, L.; Khalife, A.R.; Ge, F.; Guidi, F.; Huang, N.; Lynch, G.P.; Omori, Y.; SPT-3G Collaboration; et al. SPT-3G D1: CMB temperature and polarization power spectra and cosmology from 2019 and 2020 observations of the SPT-3G main field. *Phys. Rev.* **2026**, *113*, 083504. [CrossRef]
13. Desmond, H.; Stiskalek, R.; Nájera, J.A.; Banik, I. The subtle statistics of the distance ladder: On the distance prior and selection effects. *Mon. Not. R. Astron. Soc.* **2026**, *550*, stag1144. [CrossRef]
14. Stiskalek, R.; Desmond, H.; Tsaprazi, E.; Heavens, A.; Lavaux, G.; McAlpine, S.; Jasche, J. 1.8 per cent measurement of H_0 from Cepheids alone. *Mon. Not. R. Astron. Soc.* **2026**, *546*, staf2260. [CrossRef]
15. Stiskalek, R.; Riess, A.; Desmond, H.; Lavaux, G.; Scolnic, D. Forward-modelling Milky Way Cepheids: Selection effects and physical priors in the Gaia-HST calibration. *arXiv* **2026**, *in press*. [CrossRef]
16. Scolnic, D.; Vincenzi, M. The Role of Type Ia Supernovae in Constraining the Hubble Constant. *arXiv* **2023**, arXiv:2311.16830. [CrossRef]
17. Leavitt, H.S.; Pickering, E.C. Periods of 25 variable stars in the Magellanic Clouds. *Harv. Coll. Obs. Circ.* **1912**, *173*, 1–3.
18. Riess, A.G.; Yuan, W.; Macri, L.M.; Scolnic, D.; Brout, D.; Casertano, S.; Jones, D.O.; Murakami, Y.; Anand, G.S.; Breuval, L.; et al. A Comprehensive Measurement of the Local Value of the Hubble Constant with 1 km s^{-1} Mpc^{-1} Uncertainty from the Hubble Space Telescope and the SH0ES Team. *Astrophys. J. Lett.* **2022**, *934*, L7. [CrossRef]
19. Breuval, L.; Riess, A.G.; Casertano, S.; Yuan, W.; Macri, L.M.; Romaniello, M.; Murakami, Y.S.; Scolnic, D.; Anand, G.S.; Soszyński, I. Small Magellanic Cloud Cepheids Observed with the Hubble Space Telescope Provide a New Anchor for the SH0ES Distance Ladder. *Astrophys. J.* **2024**, *973*, 30. [CrossRef]
20. Pesce, D.W.; Braatz, J.A.; Reid, M.J.; Riess, A.G.; Scolnic, D.; Condon, J.J.; Gao, F.; Henkel, C.; Impellizzeri, C.M.V.; Kuo, C.Y.; et al. The Megamaser Cosmology Project. XIII. Combined Hubble Constant Constraints. *Astrophys. J. Lett.* **2020**, *891*, L1. [CrossRef]
21. Barua, S.; Ramakrishnan, V.; Desai, S. Determination of Hubble constant from Megamaser Cosmology Project using profile likelihood. *Astrophys. Space Sci.* **2025**, *270*, 62. [CrossRef]
22. Vogl, C.; Taubenberger, S.; Csörnyei, G.; Leibundgut, B.; Kerzendorf, W.E.; Sim, S.A.; Peterson, E.R.; Courtois, H.M.; Blondin, S.; Flörs, A.; et al. No rungs attached: A distance-ladder-free determination of the Hubble constant through type II supernova spectral modelling. *Astron. Astrophys.* **2025**, *703*, A41. [CrossRef]
23. Poulin, V.; Smith, T.L.; Karwal, T.; Kamionkowski, M. Early Dark Energy can Resolve the Hubble Tension. *Phys. Rev. Lett.* **2019**, *122*, 221301. [CrossRef] [PubMed]
24. Poulin, V.; Smith, T.L.; Karwal, T. The Ups and Downs of Early Dark Energy solutions to the Hubble tension: A review of models, hints and constraints circa 2023. *Phys. Dark Universe* **2023**, *42*, 101348. [CrossRef]
25. Mirpoorian, S.H.; Jedamzik, K.; Pogosian, L. Is dynamical dark energy necessary? DESI BAO and modified recombination. *J. Cosmol. Astropart. Phys.* **2025**, *2025*, 050. [CrossRef]
26. Bernal, J.L.; Verde, L.; Jimenez, R.; Kamionkowski, M., Valcin, D.; Wandelt, B.D. Trouble beyond H_0 and the new cosmic triangles. *Phys. Rev.* **2021**, *103*, 103533. [CrossRef]
27. Valcin, D.; Bernal, J.L.; Jimenez, R.; Verde, L.; Wandelt, B.D. Inferring the age of the universe with globular clusters. *J. Cosmol. Astropart. Phys.* **2020**, *2020*, 002. [CrossRef]
28. Montalbán, J.; Mackereth, J.T.; Miglio, A.; Vincenzo, F.; Chiappini, C.; Buldgen, G.; Mosser, B.; Noels, A.; Scuflaire, R.; Vrard, M.; et al. Chronologically dating the early assembly of the Milky Way. *Nat. Astron.* **2021**, *5*, 640–647. [CrossRef]
29. Valcin, D.; Jimenez, R.; Verde, L.; Bernal, J.L.; Wandelt, B.D. The age of the Universe with globular clusters: Reducing systematic uncertainties. *J. Cosmol. Astropart. Phys.* **2021**, *2021*, 017. [CrossRef]

30. Limberg, G.; Souza, S.O.; Pérez-Villegas, A.; Rossi, S.; Perottoni, H.D.; Santucci, R.M. Reconstructing the disrupted dwarf galaxy gaia-sausage/enceladus using its stars and globular clusters. *Astrophys. J.* **2022**, *935*, 109. [CrossRef]
31. Xiang, M.; Rix, H.-W. A time-resolved picture of our Milky Way's early formation history. *Nature* **2022**, *603*, 599–603. [CrossRef] [PubMed]
32. Cimatti, A.; Moresco, M. Revisiting the Oldest Stars as Cosmological Probes: New Constraints on the Hubble Constant. *Astrophys. J.* **2023**, *953*, 149. [CrossRef] [PubMed]
33. Nepal, S.; Chiappini, C.; Queiroz, A.B.; Guiglion, G.; Montalbán, J.; Steinmetz, M.; Miglio, A.; Khalatyan, A. Discovery of the local counterpart of disc galaxies at z > 4: The oldest thin disc of the Milky Way using *Gaia*-RV. *Astron. Astrophys.* **2024**, *688*, A167. [CrossRef]
34. Souza, S.O.; Libralato, M.; Nardiello, D.; Kerber, L.O.; Ortolani, S.; Pérez-Villegas, A.; Oliveira, R.A.P.; Barbuy, B.; Bica, E.; Griggio, M.; et al. Combined Gemini-South and HST photometric analysis of the globular cluster NGC 6558—The age of the metal-poor population of the Galactic bulge. *Astron. Astrophys.* **2024**, *690*, A37. [CrossRef]
35. Lundkvist, M.S.; Larsen, J.R.; Li, Y.; Winther, M.L.; Bedding, T.R.; Kjeldsen, H.; White, T.R.; Nielsen, M.B.; Buldgen, G.; Guillaume, C.; et al. Asteroseismic investigation of HD 140283: The Methuselah star. *Astron. Astrophys.* **2025**, *703*, A232.. [CrossRef]
36. Valcin, D.; Jimenez, R.; Seljak, U.; Verde, L. The age of the universe with globular clusters. Part III. Gaia distances and hierarchical modeling. *J. Cosmol. Astropart. Phys.* **2025**, *2025*, 030. [CrossRef]
37. Xiang, M.; Rix, H.-W.; Yang, H.; Liu, J.; Huang, Y.; Frankel, N. The formation and survival of the Milky Way's oldest stellar disk. *Nat. Astron.* **2025**, *9*, 101–110. [CrossRef]
38. Banik, I.; Kudakolawa Kaluarachchige, T.; Cookson, S.; Desmond, H. The age of the Universe from a large sample of the oldest Galactic stars. *arXiv* **2026**, arXiv:2607.00764. [CrossRef]
39. Shariat, C.; El-Badry, K.; Bhattacharjee, S. How precisely can we measure the ages of subgiant and giant stars? *Open J. Astrophys.* **2026**, *9*, 162534. [CrossRef]
40. Tomasetti, E.; Chiappini, C.; Nepal, S.; Moresco, M.; Lardo, C.; Cimatti, A.; Anders, F.; Queiroz, A.B.A.; Limberg G. The oldest Milky Way stars: New constraints on the age of the Universe and the Hubble constant. *Astron. Astrophys.* **2026**, *707*, A111. [CrossRef]
41. Valcin, D.; Jimenez, R.; Lardo, C.; Seljak, U.; Verde, L. The Age of the Universe with Globular Clusters IV: Multiple Stellar Populations. *arXiv* **2026**, arXiv:2603.04872. [CrossRef]
42. Cogato, F.; Moresco, M.; Amati, L.; Cimatti, A. An analytical late–Universe approach to the weaving of modern cosmology. *Mon. Not. R. Astron. Soc.* **2024**, *527*, 4874–4888. [CrossRef]
43. Guo, W.; Wang, Q.; Cao, S.; Biesiada, M.; Liu, T.; Lian, Y.; Jiang, X.; Mu, C.; Cheng, D. Newest Measurements of Hubble Constant from DESI 2024 Baryon Acoustic Oscillation Observations. *Astrophys. J. Lett.* **2025**, *978*, L33. [CrossRef]
44. Banik, I.; Samaras, N. Constraints on the Hubble and Matter Density Parameters with and Without Modelling the CMB Anisotropies. *Astronomy* **2025**, *4*, 24. [CrossRef]
45. Tristram, M.; Banday, A.J.; Douspis, M.; Garrido, X.; Górski, K.M.; Henrot-Versillé, S.; Hergt, L.T.; Ilić, S.; Keskitalo, R.; Lagache, G.; et al. Cosmological parameters derived from the final *Planck* data release (PR4). *Astron. Astrophys.* **2024**, *682*, A37. [CrossRef]
46. Calabrese, E.; Hill, J.C.; Jense, H.T.; La Posta, A.; Abril-Cabezas, I.; Addison, G.E.; Ade, P.A.R.; Aiola, S.; Alford, T.; Alonso, D.; et al. The Atacama Cosmology Telescope: DR6 constraints on extended cosmological models. *J. Cosmol. Astropart. Phys.* **2025**, *2025*, 063. [CrossRef]
47. Vagnozzi, S. Seven Hints That Early-Time New Physics Alone Is Not Sufficient to Solve the Hubble Tension. *Universe* **2023**, *9*, 393. [CrossRef]
48. Giovanetti, C. A generic ωb tension in early-time solutions to the Hubble tension. *arXiv* **2026**, arXiv:2604.05095. [CrossRef]
49. Launders, T.; Giovanetti, C.; Liu, H. A data-driven prediction for the primordial deuterium abundanc. *arXiv* **2026**, arXiv:2604.16600. [CrossRef]
50. Abdul Karim, M.; Aguilar, J.; Ahlen, S.; Alam, S.; Allen, L.; Allende Prieto, C.; Alves, O.; Anand, A.; Andrade, U.; DESI Collaboration; et al. DESI DR2 results. II. Measurements of baryon acoustic oscillations and cosmological constraints. *Phys. Rev.* **2025**, *112*, 083515. [CrossRef]
51. Chen, S.-F.; Howlett, C.; White, M.; McDonald, P.; Ross, A.J.; Seo, H.-J.; Padmanabhan, N.; Aguilar, J.; Ahlen, S.; Alam, S.; et al. Baryon acoustic oscillation theory and modelling systematics for the DESI 2024 results. *Mon. Not. R. Astron. Soc.* **2024**, *534*, 544–574. [CrossRef]
52. Banik, I.; Kalaitzidis, V. Testing the local void hypothesis using baryon acoustic oscillation measurements over the last 20 yr. *Mon. Not. R. Astron. Soc.* **2025**, *540*, 545–561. [CrossRef]
53. Nájera, J.A.; Banik, I.; Desmond, H.; Kalaitzidis, V. Comparing Measures of the Hubble and BAO Tensions in ΛCDM and Possible Solutions in $f(Q)$ Gravity. *Galaxies* **2026**, *14*, 19. [CrossRef]
54. Zhao, H.; Peacock, J.A.; Li, B. Testing gravity theories via transverse Doppler and gravitational redshifts in galaxy clusters. *Phys. Rev. D* **2013**, *188*, 043013. [CrossRef]

55. Wu, H.-Y.; Huterer, D. Sample variance in the local measurements of the Hubble constant. *Mon. Not. R. Astron. Soc.* **2017**, *471*, 4946–4955. [CrossRef]
56. Camarena, D.; Marra, V. Impact of the cosmic variance on H_0 on cosmological analyses. *Phys. Rev.* **2018**, *98*, 023537. [CrossRef]
57. Maddox, S.J.; Efstathiou, G.; Sutherland, W.J.; Loveday J. The power spectrum of IRAS galaxies. *Mon. Not. R. Astron. Soc.* **1990**, *242*, 43P–47P. [CrossRef]
58. Shanks, T. The Galactic and Extragalactic Background Radiation; In *International Astronomical Union Symposium*; Bowyer, S., Leinert, C., Eds; Springer: Dordrecht, The Netherlands, 1990; Volume 139, pp. 269–281.
59. Keenan, R.C.; Barger, A.J.; Cowie, L.L. Evidence for a ∼300 megaparsec scale under-density in the local galaxy distribution. *Astrophys. J.* **2013**, *775*, 62. [CrossRef]
60. Böhringer, H.; Chon, G.; Bristow, M.; Collins, C.A. The extended ROSAT-ESO Flux-Limited X-ray Galaxy Cluster Survey (REFLEX II). *Astron. Astrophys.* **2015**, *574*, A26. [CrossRef]
61. Böhringer, H.; Chon, G.; Collins, C.A. Observational evidence for a local underdensity in the Universe and its effect on the measurement of the Hubble constant. *Astron. Astrophys.* **2020**, *636*, A19. [CrossRef]
62. Rubart, M.; Schwarz, D.J. Cosmic radio dipole from NVSS and WENSS. *Astron. Astrophys.* **2013**, *555*, A117. [CrossRef]
63. Rubart, M.; Bacon, D.; Schwarz, D.J. Impact of local structure on the cosmic radio dipole. *Astron. Astrophys.* **2014**, *565*, A111. [CrossRef]
64. Huang, J.S.; Cowie, L.L.; Gardner, J.P.; Hu, E.M.; Songaila, A.; Wainscoat, R.J. The Hawaii K-Band Galaxy Survey. II. Bright *K*-Band Imaging. *Astrophys. J.* **1997**, *476*, 12. [CrossRef] [PubMed]
65. Busswell, G.S.; Shanks, T.; Frith, W.J.; Outram, P.J.; Metcalfe, N.; Fong, R. The local hole in the galaxy distribution: New optical evidence. *Mon. Not. R. Astron. Soc.* **2004**, *354*, 991. [CrossRef]
66. Frith, W.J.; Busswell, G.S.; Fong, R.; Metcalfe, N.; Shanks, T. The local hole in the galaxy distribution: Evidence from 2MASS. *Mon. Not. R. Astron. Soc.* **2003**, *345*, 1049–1056. [CrossRef]
67. Frith, W.J.; Shanks, T.; Outram, P.J. 2MASS constraints on the local large-scale structure: A challenge to ΛCDM? *Mon. Not. R. Astron. Soc.* **2005**, *361*, 701–709. [CrossRef]
68. Frith, W.J.; Metcalfe, N.; Shanks, T. New *H*-band galaxy number counts: A large local hole in the galaxy distribution. *Mon. Not. R. Astron. Soc.* **2006**, *371*, 1601–1609. [CrossRef]
69. Whitbourn, J.R.; Shanks, T. The local hole revealed by galaxy counts and redshifts. *Mon. Not. R. Astron. Soc.* **2014**, *437*, 2146–2162. [CrossRef]
70. Whitbourn, J.R.; Shanks, T. The galaxy luminosity function and the Local Hole. *Mon. Not. R. Astron. Soc.* **2016**, *459*, 496–507. [CrossRef]
71. Wong, J.H.W.; Shanks, T.; Metcalfe, N.; Whitbourn, J.R. The local hole: A galaxy underdensity covering 90 per cent of sky to ≈200 Mpc. *Mon. Not. R. Astron. Soc.* **2022**, *511*, 5742–5755. [CrossRef]
72. Tao, B.; Zhang, H.-X.; Wang, W.; Wang, E.; Chen, G.; Wang, H.; Chen, L.; Chen, Q.-H.; Huang, S.; Kong, X.; et al. The First Systematic Survey of Stellar Halos in High-inclination Galaxies Reveals Unusually Quiescent Merger Histories of Nearby Galaxies. *Astrophys. J. Suppl. Ser.* **2026**, *284*, 31. [CrossRef]
73. Haslbauer, M.; Banik, I.; Kroupa, P. The KBC void and Hubble tension contradict ΛCDM on a Gpc scale—Milgromian dynamics as a possible solution. *Mon. Not. R. Astron. Soc.* **2020**, *499*, 2845–2883. [CrossRef]
74. Milgrom, M. A modification of the Newtonian dynamics as a possible alternative to the hidden mass hypothesis. *Astrophys. J.* **1983**, *270*, 365–370. [CrossRef] [PubMed]
75. Futamase, T.; Kojima, R.; Tomonaga, M. Reconstructing a large-scale matter-density contrast profile to reconcile Pantheon + supernovae with DESI DR2 BAO observations in an inhomogeneous universe. *Phys. Rev. D* **2026**, *113*, 103515. [CrossRef]
76. Banik, I.; Desmond, H.; Kalaitzidis, V.; Mazurenko, S. The local void model for the Hubble and BAO tensions. *arXiv* **2026**, arXiv:2602.03928. [CrossRef]
77. Ivanov, M.M.; Ali-Haïmoud, Y.; Lesgourgues, J. H_0 tension or T_0 tension?. *Phys. Rev. D* **2020**, *102*, 063515. [CrossRef]
78. Stiskalek, R.; Desmond, H.; Banik, I. Testing the local supervoid solution to the Hubble tension with direct distance tracers. *Mon. Not. R. Astron. Soc.* **2025**, *543*, 1556–1573. [CrossRef]
79. Jimenez, R.; Loeb A. Constraining Cosmological Parameters Based on Relative Galaxy Ages. *Astrophys. J.* **2002**, *573*, 37. [CrossRef] [PubMed]
80. Moresco, M.; Jimenez, R.; Verde, L.; Pozzetti, L.; Cimatti, A.; Citro, A. Setting the Stage for Cosmic Chronometers. I. Assessing the Impact of Young Stellar Populations on Hubble Parameter Measurements. *Astrophys. J.* **2018**, *868*, 84. [CrossRef]
81. Moresco, M.; Jimenez, R.; Verde, L.; Cimatti, A.; Pozzetti, L. Setting the Stage for Cosmic Chronometers. II. Impact of Stellar Population Synthesis Models Systematics and Full Covariance Matrix. *Astrophys. J.* **2020**, *898*, 82. [CrossRef]
82. Moresco, M. Measuring the expansion history of the Universe with cosmic chronometers. *arXiv* **2024**, arXiv:2412.01994. [CrossRef]
83. Wang, Z.; Lei, L.; Fan, Y. New $H(z)$ Measurement at Redshift = 0.12 with DESI Data Release 1. *Astrophys. J.* **2026**, *1003*, 81. [CrossRef]

84. Fixsen, D.J. The Temperature of the Cosmic Microwave Background. *Astrophys. J.* **2009**, *707*, 916. [CrossRef]
85. Yoo J.; Mitsou E.; Dirian Y.; Durrer R. Background photon temperature $\bar{T}$: A new cosmological Parameter? *Phys. Rev. D* **2019**, *100*, 063510. [CrossRef]
86. Lemos, P.; Lewis, A. CMB constraints on the early Universe independent of late-time cosmology. *Phys. Rev.* 2023, 107, 103505. [CrossRef]
87. Blas, D.; Lesgourgues, J.; Tram, T. The Cosmic Linear Anisotropy Solving System (CLASS). Part II: Approximation schemes. *J. Cosmol. Astropart. Phys.* **2011**, *2011*, 034. [CrossRef]
88. Alpher, R.A.; Bethe, H.; Gamow, G. The origin of chemical elements. *Phys. Rev.* **1948**, *73*, 803. [CrossRef]
89. Tytler, D.; O'Meara, J.M.; Suzuki, N.; Lubin, D. Review of Big Bang Nucleosynthesis and Primordial Abundances. *Phys. Scr.* **2000**, *85*, 12. [CrossRef]
90. Cyburt, R.H.; Fields, B.D.; Olive, K.A.; Yeh, T.-H. Big Bang Nucleosynthesis: Present status. *Rev. Mod. Phys.* **2016**, *88*, 015004. [CrossRef]
91. Pettini, M.; Cooke, R. Precision cosmology with the lightest elements. *Astrophys. Space Sci.* **2026**, *371*, 20. [CrossRef]
92. Pitrou, C.; Coc, A.; Uzan, J.-P.; Vangioni, E. Precision big bang nucleosynthesis with improved Helium-4 predictions. *Phys. Rep.* **2018**, *754*, 1–66. [CrossRef]
93. Cooke, R.J.; Pettini, M.; Steidel, C.C. One Percent Determination of the Primordial Deuterium Abundance. *Astrophys. J.* **2018**, *855*, 102. [CrossRef]
94. Aver, E.; Olive, K.A.; Skillman, E.D. The effects of He I λ10830 on helium abundance determinations. *J. Cosmol. Astropart. Phys.* **2015**, *2015*, 011. [CrossRef]
95. Giovanetti, C.; Lisanti, M.; Liu, H.; Mishra-Sharma, S.; Ruderman, J.T. Cosmological parameter estimation with a joint-likelihood analysis of the cosmic microwave background and big bang nucleosynthesis. *Phys. Rev. D* **2025**, *112*, 063530. [CrossRef]
96. Abbott, T.M.C.; Acevedo, M.; Aguena, M.; Alarcon, A.; Allam, S.; Alves, O.; Amon, A.; Andrade-Oliveira, F.; Annis, J.; DES Collaboration; et al. The Dark Energy Survey: Cosmology Results with ∼1500 New High-redshift Type Ia Supernovae Using the Full 5 yr Data Set. *Astrophys. J. Lett.* **2024**, *973*, L14. [CrossRef]
97. Popovic, B.; Shah, P.; Kenworthy, W.D.; Kessler, R.; Davis, T.M.; Goobar, A.; Scolnic, D.; Vincenzi, M.; Wiseman, P.; Chen, R.; et al. The Dark Energy Survey supernova program: A reanalysis of cosmology results and evidence for evolving dark energy with an updated Type Ia supernova calibration. *Mon. Not. R. Astron. Soc.* **2026**, *548*, stag63. [CrossRef]
98. Skilling, J. Bayesian Inference and Maximum Entropy Methods in Science and Engineering. In *American Institute of Physics Conference Series Vol. 735, Proceedings of the 24th International Workshop on Bayesian Inference and Maximum Entropy Methods in Science and Engineering, Jarinu, Brazil, 9–14 July 2004*; Fischer, R., Preuss, R., Toussaint, U.V., Eds.; AIP: College Park, MD, USA; pp. 395–405.. [CrossRef]
99. Skilling, J. Nested sampling for general Bayesian computation . *Bayesian Anal.* **2006**, *1*, 833–859. [CrossRef]
100. Feroz, F.; Hobson, M.P.; Bridges, M. MultiNest: An efficient and robust Bayesian inference tool for cosmology and particle physics. *Mon. Not. R. Astron. Soc.* **2009**, *398*, 1601. [CrossRef]
101. Speagle, J.S. DYNESTY: A dynamic nested sampling package for estimating Bayesian posteriors and evidences. *Mon. Not. R. Astron. Soc.* **2020**, *493*, 3132–3158. [CrossRef]
102. Koposov, S.; Speagle, J.; Barbary, K.; Ashton, G.; Bennett, E.; Buchner, J.; Scheffler, C.; Cook, B.; Talbot, C.; Guillochon, J.; et al. *Joshspeagle/dynesty*, Version v2.1.4; Zenodo: Geneva, Switzerland, 2024. [CrossRef]
103. Lewis, A. GetDist: A Python package for analysing Monte Carlo samples. *J. Cosmol. Astropart. Phys.* **2025**, *2025*, 025. [CrossRef]
104. Percival, W.J.; Sutherland, W.; Peacock, J.A.; Baugh, C.M.; Bland-Hawthorn, J.; Bridges, T.; Cannon, R.; Cole, S.; Colless, M.; Collins, C.; et al. Parameter constraints for flat cosmologies from cosmic microwave background and 2dFGRS power spectra. *Mon. Not. R. Astron. Soc.* 2002, 337, 1068–1080. [CrossRef]
105. Kable, J.A.; Addison, G.E.; Bennett, C.L. Quantifying the CMB Degeneracy between the Matter Density and Hubble Constant in Current Experiments. *Astrophys. J.* **2019**, *871*, 77. [CrossRef]
106. Lewis, A.; Chamberlain, E. Understanding acoustic scale observations: The one-sided fight against Λ. *J. Cosmol. Astropart. Phys.* **2025**, *2025*, 065. [CrossRef]
107. Kamalinejad, F.; Slepian, Z.; Krolewski, A.; Greco, A.; Leonard, W.O.; Chellino, J.; Reinhard, M.; Fernández-García, E.; Prada, F.; Aguilar, J.; et al. First Detection of the Baryon Acoustic Oscillation (BAO) Feature in the 3-Point Correlation Function of DESI DR1 Luminous Red Galaxies. *arXiv* **2026**, arXiv:2602.16134. [CrossRef]
108. Jia, X.D.; Hu, J.P.; Wang, F.Y., Evidence of a decreasing trend for the Hubble constant. *Astron. Astrophys.* **2023**, *674*, A45. [CrossRef]
109. Jia, X.D.; Hu, J.P.; Yi, S.X.; Wang, F.Y. Uncorrelated Estimations of H0 Redshift Evolution from DESI Baryon Acoustic Oscillation Observations. *Astrophys. J. Lett.* **2025**, *979*, L34. [CrossRef]
110. Jia, X.D.; Hu, J.P.; Gao, D.H.; Yi, S.X.; Wang, F.Y. The Hubble Tension Resolved by the DESI Baryon Acoustic Oscillations Measurements. *Astrophys. J. Lett.* **2025**, *994*, L22. [CrossRef]

111. Krishnan, C.; Colgáin, E.Ó.; Ruchika, Sen, A.A.; Sheikh-Jabbari, M.M.; Yang, T. Is there an early Universe solution to Hubble tension? *Phys. Rev. D* **2020**, *102*, 103525. [CrossRef]
112. Krishnan, C.; Colgáin, E.Ó.; Sheikh-Jabbari, M.M.; Yang, T. Running Hubble tension and a H0 diagnostic. *Phys. Rev. D* **2021**, *103*, 103509. [CrossRef]
113. Jia, X.-D.; Dai, X.-Y.; Yang, Y.-P.; Wang, F.-Y. A Review on Resolving the Hubble Tension via Late-Universe Physics. *Galaxies* **2026**, *14*, 55. [CrossRef]
114. Lopez-Hernandez, M.; De-Santiago, J. Is there a dynamical tendency in H_0 with late time measurements? *J. Cosmol. Astropart. Phys.* **2025**, *2025*, 026. [CrossRef]
115. Sachs, R.K.; Wolfe, A.M. Perturbations of a Cosmological Model and Angular Variations of the Microwave Background. *Astrophys. J.* **1967**, *147*, 73. [CrossRef] [PubMed]
116. Asencio, E.; Banik, I.; Kroupa, P. A massive blow for ΛCDM—The high redshift, mass, and collision velocity of the interacting galaxy cluster El Gordo contradicts concordance cosmology. *Mon. Not. R. Astron. Soc.* **2021**, *500*, 5249–5267.. [CrossRef]
117. Asencio, E.; Banik, I.; Kroupa, P. The El Gordo Galaxy Cluster Challenges ΛCDM for Any Plausible Collision Velocity. *Astrophys. J.* **2023**, *954*, 162. [CrossRef]
118. Secrest, N.J.; von Hausegger, S.; Rameez, M.; Mohayaee, R.; Sarkar, S.; Colin, J. A Test of the Cosmological Principle with Quasars. *Astrophys. J. Lett.* **2021**, *908*, L51. [CrossRef]
119. Secrest, N.J.; von Hausegger, S.; Rameez, M.; Mohayaee, R.; Sarkar, S. A Challenge to the Standard Cosmological Model. *Astrophys. J. Lett.* **2022**, *937*, L31. [CrossRef]
120. Dam, L.; Lewis, G.F.; Brewer, B.J. Testing the cosmological principle with CatWISE quasars: A bayesian analysis of the number-count dipole. *Mon. Not. R. Astron. Soc.* **2023**, *525*, 231–245. [CrossRef]
121. Wagenveld, J.D.; Klöckner, H.-R.; Gupta, N.; Sekhar, S.; Jagannathan, P.; Deka, P.P.; Jose, J.; Balashev, S.A.; Borgaonkar, D.; Chatterjee, A.; et al. The MeerKAT Absorption Line Survey Data Release 2: Wideband continuum catalogues and a measurement of the cosmic radio dipole. *Astron. Astrophys.* **2024**, *690*, A163. [CrossRef]
122. Oayda, O.T.; Lewis, G.F. Wising up to CatWISE: Using simulation-based inference to interpret the ecliptic bias and confirm the cosmic dipole excess. *Mon. Not. R. Astron. Soc.* **2026**, *546*, stag248. [CrossRef]
123. Gandhi, A. Intrinsic dipole anisotropies and the Hubble tension: A unified theoretical framework for correlated large-scale modes. *Mon. Not. R. Astron. Soc.* **2026**, *548*, stag582. [CrossRef]
124. Russell, A.; Banik, I.; Cray, O.; Zhao, H. How does a MOND cosmology fare on Gpc scales?—Collisionless N-body simulations of νHDM. *Mon. Not. R. Astron. Soc.* **2026**, *547*, stag399. [CrossRef]
125. Nunes, N.J.; Mota, D.F. Structure formation in inhomogeneous dark energy models. *Mon. Not. R. Astron. Soc.* **2006**, *368*, 751–758. [CrossRef]
126. Sunyaev, R.A.; Zeldovich, I.B. Microwave Background Radiation as a Probe of the Contemporary Structure and History of the Universe. *Annu. Rev. Astron. Astrophys.* **1980**, *18*, 537–560. [CrossRef]
127. Ding, Q.; Nakama, T.; Wang, Y. A gigaparsec-scale local void and the Hubble tension. *Sci. China Phys. Mech. Astron.* **2020**, *63*, 290403. [CrossRef]
128. Cai, T.; Ding, Q.; Wang, Y. Reconciling cosmic dipolar tensions with a gigaparsec void. *Phys. Rev.* **2025**, *111*, 103502. [CrossRef]
129. Singal, A.K. Discordance of dipole asymmetries seen in recent large radio surveys with the cosmological principle. *Mon. Not. R. Astron. Soc.* **2023**, *524*, 3636. [CrossRef]
130. Bashir, M.; Chingangbam, P.; Appleby, S. The CatWISE2020 Quasar Dipole: A Reassessment of the Cosmic Dipole Anomaly. *Astrophys. J.* **2026**, *1003*, 162. [CrossRef]
131. Wagenveld, J.D.; von Hausegger, S.; Klöckner, H.-R.; Schwarz, D.J. The kinematic contribution to the cosmic number count dipole. *Astron. Astrophys.* **2025**, *697*, A112. [CrossRef]
132. Tully, R.B.; Kourkchi, E.; Courtois, H.M.; Anand, G.S.; Blakeslee, J.P.; Brout, D.; de Jaeger, T.; Dupuy, A.; Guinet, D.; Howlett, C.; et al. Cosmicflows-4. *Astrophys. J.* **2023**, *944*, 94. [CrossRef]
133. Akita, K.; Yamaguchi, M. A precision calculation of relic neutrino decoupling. *J. Cosmol. Astropart. Phys.* **2020**, *2020*, 012. [CrossRef]
134. Froustey, J.; Pitrou, C.; Volpe, M.C. Neutrino decoupling including flavour oscillations and primordial nucleosynthesis. *J. Cosmol. Astropart. Phys.* **2020**, *2020*, 015. [CrossRef]
135. Bennett, J.J.; Buldgen, G.; de Salas, P.F.; Drewes, M.; Gariazzo, S.; Pastor, S.; Wong, Y.Y.Y. Towards a precision calculation of the effective number of neutrinos Neff in the Standard Model. Part II. Neutrino decoupling in the presence of flavour oscillations and finite-temperature QED. *J. Cosmol. Astropart. Phys.* **2021**, *2021*, 073. [CrossRef]
136. Lesgourgues, J.; Pastor, S. Neutrino Mass from Cosmology. *Adv. High Energy Phys.* **2012**, *2012*, 608515. [CrossRef]

137. Komatsu, E.; Smith, K.M.; Dunkley, J.; Bennett, C.L.; Gold, B.; Hinshaw, G.; Jarosik, N.; Larson, D.; Nolta, M.R.; Page, L.; et al. Seven-year wilkinson microwave anisotropy probe (WMAP) observations: Cosmological interpretation. *Astrophys. J. Suppl. Ser.* **2011**, *192*, 18. [CrossRef]
138. Abusleme, A.; Adam, T.; Ahmad, S.; Ahmed, R.; Aiello, S.; Akram, M.; Aleem, A.; An, F.; An, Q.; Juno Collaboration; et al. Potential to identify neutrino mass ordering with reactor antineutrinos at JUNO. *Chin. Phys. C* **2025**, *49*, 033104. [CrossRef]

Disclaimer/Publisher's Note: The statements, opinions and data contained in all publications are solely those of the individual author(s) and contributor(s) and not of MDPI and/or the editor(s). MDPI and/or the editor(s) disclaim responsibility for any injury to people or property resulting from any ideas, methods, instructions or products referred to in the content.